DISSERTATION

MULTIFREQUENCY RETRIEVAL OF CLOUD ICE

PARTICLE SIZE DISTRIBUTIONS

Submitted by

Brian D. Griffith

Department of Atmospheric Science

In partial fulfillment of the requirements

For the Degree of Doctor of Philosophy

Colorado State University

Fort Collins, Colorado

Fall 2005

COLORADO STATE UNIVERSITY

September 20, 2005

WE HEREBY RECOMMEND THAT THE DISSERTATION PREPARED UNDER OUR SUPERVISION BY BRIAN D. GRIFFITH ENTITLED MULTIFREQUENCY RETRIEVAL OF CLOUD ICE PARTICLE SIZE DISTRIBUTIONS BE ACCEPTED AS FULFILLING IN PART REQUIREMENTS FOR THE DEGREE OF DOCTOR OF PHILOSOPHY.

Committee on Graduate Work

Adviser

Department Head

ABSTRACT OF DISSERTATION

MULTIFREQUENCY RETRIEVAL OF CLOUD ICE

PARTICLE SIZE DISTRIBUTIONS

There are many sources of uncertainty in remote sensing retrievals. This is particularly true where complex parameters such as liquid or ice hydrometeors must be retrieved. Many of the uncertainties are the direct result of assumptions made in the retrieval process to address the ill-posed nature of the inverse problem – namely that there are more variables than measurements. In this paper, an optimal estimation retrieval technique is applied to a multi-frequency data set from the Wakasa Bay AMSR-E validation experiment. First, airborne radar observations at 13.4, 35.6 and 94.9 GHz are integrated to retrieve all three parameters of a normalized gamma ice particle size distribution (PSD), N_o*, μ, and D_m. This retrieved PSD was validated against the near-simultaneous coincident *in situ* cloud probe observations. The differences between the retrieved and *in situ* measured PSDs were explored through sensitivity analysis and the sources of uncertainty were found to be the ice particle density and the aspect ratio of the nonspherical particles modeled as oblate spheroids in the forward radiative transfer model. The optimal estimation technique was then applied to retrieve an optimal density and aspect ratio for the cloud under study through integration of the *in situ* and remote

sensing observations. The optimal particle size-density relationship was found to be $\rho(D) = 0.07 * D^{-1.58}$ and the oblate spheroid aspect ratio was found to be 0.53. The use of these optimal values as improved assumptions in the PSD retrieval reduced the uncertainty in the retrieved reflectivity of the three radars from +/– 6 dB to +/– 2 dB. Next, the retrieval technique is expanded to include passive microwave observations and retrieve a full atmospheric column vertical hydrometeor profile. Eleven airborne passive microwave frequencies from 10.7 to 340 GHz are integrated with airborne radar observations at 13.4, 35.6 and 94.9 GHz to retrieve all three parameters of a normalized gamma ice particle size distribution (PSD): N_o^*, μ, and D_m. The vertical profile retrieval is validated against a clear sky scene before being applied to the horizontal extent of an ice cloud. The PSD retrieval shows vertical structure consistent with cloud microphysical processes. The default density and shape retrieval is used as a baseline for comparison with the retrieval using the optimized model from the companion paper, which reveals an order of magnitude difference in ice water path between the two retrievals. This difference is explored and an information content analysis reveals that the optimized model improves on the information content of the retrieval by 2^{87} more states resolved than the default model indicating a significant reduction in retrieval uncertainty.

Brian D. Griffith

Atmospheric Science Department

Colorado State University

Fort Collins, CO 80523

Fall 2005

ACKNOWLEDGEMENTS

I would first like to thank my adviser, Professor Christian Kummerow for his guidance and leadership throughout this process. I would also like to thank the United States Air Force, Air Force Institute of Technology Civilian Institution program for allowing the opportunity to complete this Ph. D. research program. Thanks to Dr. Masataka Murakami, Japanese Meteorological Research Institute for supplying the Japanese Cloud Probe data and his explanations of the measurements. Thanks also to Dr. Richard Austin, Dr. Simone Tanelli, Dr. Jim Wang and Dr. Thomas T. Wilheit for their contributions to the Wakasa Bay data set and my use of it. Thanks to Dr. Tristan L'Ecuyer for his seemingly endless patience in discussing all aspects of the optimal estimation retrieval. Thanks to Becky Burke and the rest of the Kummerow research group. Finally, I'd like to thank my wife Robyn for her unfailing support and encouragement.

TABLE OF CONTENTS

LIST OF TABLES

LIST OF FIGURES

CHAPTER 1

INTRODUCTION

Clouds are a fundamental component of the water cycle in the atmosphere. They dominate the planetary energy budget through cooling the earth by reflecting sunlight back to space and warming the earth by absorbing and emitting thermal radiation. By modulating the energy budget, clouds fundamentally alter the general atmospheric and oceanic circulations.

Unfortunately, there are many sources of uncertainty in remote sensing retrievals. Instruments, measurement techniques, and the physical models relating the measured values to the parameters of interest and to each other all have intrinsic uncertainties. Many of those uncertainties are the result of assumptions made in the retrieval process. While these assumptions are necessary to solve the under-constrained retrieval problem, they can affect not only the output uncertainty but also the character of the retrieved solution itself.

Retrievals of cloud or rainfall parameters intrinsically have more free parameters than are routinely observed. As a result, the largest retrieval uncertainty is generally not in the observation (sensor noise) but in the forward model used for the inversion. These forward model uncertainties are not well defined and little is known about them (AMSR Rainfall Validation Implementation Strategy, 2001). Exploring and quantifying the

assumptions in the forward model and the resulting uncertainty in the retrieval is thus essential to developing confidence in remote sensing measurements.

State-of-the-art passive microwave retrievals of raining clouds use a Bayesian scheme to match observed brightness temperatures against a database of cloud-resolving model vertical profiles (Kummerow et al., 2001). However, there are more independent variables than there are channels in the observing system. Thus, these schemes are unable to determine the vertical structure of clouds and rainfall with vertical resolutions required as inputs for many global climate models (L'Ecuyer and Stephens, 2002). Spaceborne radars, as on the Tropical Rainfall Measuring Mission (TRMM) or CloudSat satellites, have the capability to add vertical structure information to complement the passive microwave retrieval.

Radars are able to return detailed information about the distribution of scattering targets along the ray path. For vertically oriented radars, this means that a vertical profile of hydrometeors can be retrieved. The power returned to the radar is a function of the density, shape, phase, orientation and size of the target. Precise description of the particle size distribution (PSD) is essential to relating the physical properties of individual particles to the physical properties of the volume being observed (Viltard et al., 2000). However, single-frequency spaceborne radars like the TRMM precipitation radar (PR) or CloudSat radar must assume the PSD or find ancillary information to complete the retrieval. Berg et al. (2002) found significant systematic regional biases between the TRMM PR and the TRMM Microwave Imager (TMI) rainfall estimates. They asserted that the biases stem directly from the assumptions needed to retrieve rainfall in the fundamentally under-constrained framework in which each sensor must operate.

Current research areas focusing on reducing the uncertainty in cloud and rainfall retrievals address these underlying assumptions in different ways. One focus is to retrieve vertical structure with radar while using a radiometric estimate of column water or ice as a constraint. Frisch et al. (1998) used cloud radar and microwave radiometer measurements to deduce cloud liquid water profiles. Austin and Stephens (2001) described an algorithm for the detection of stratus clouds through a combination of radar and visible optical depth using the optical depth information as a constraint on the radar retrieval. A variation on this theme was introduced by Masunaga and Kummerow (2005) where TRMM PR-retrieved PSDs were adjusted to better match TRMM TMI microwave brightness temperatures. Despite advances in our ability to retrieve PSD parameters from the combination of two sensors, these retrievals still require an assumption about PSD, particle density, and particle shape, naming only the most important parameters, as there remain more unknowns than observations.

Another thrust in combined active/passive hydrometeor retrieval research involves developing more precise median representative PSDs sorted by scene or class (e.g., convective or stratiform) for application directly into the forward model as an improved assumption (L'Ecuyer et al., 2004). However, PSDs vary from storm to storm and even within the same storm (Atlas et al., 1995). While such classes may be an improvement, they still leave a fundamental uncertainty in the retrieval of instantaneous vertical hydrometeor structure. The under-constrained nature of current retrieval algorithms prevents an accurate measurement. In addition, the lack of realistic and verifiable error estimates makes it impossible to validate the hydrometeor retrieval in a physical sense.

An algorithm for retrieving profiles from spaceborne radar that can be adapted to any PSD was introduced by L'Ecuyer and Stephens (2002). This algorithm employs an optimal estimation theory framework and is adaptable to multiple instrument observations. In addition, it provides for a rigorous treatment of the uncertainties in the retrieved profile with a full set of error diagnostics. This explicit treatment of profile uncertainties is required for algorithm verification, model validation and data assimilation applications (L'Ecuyer and Stephens, 2002). This optimal estimation algorithm will serve as a template for incorporating an unprecedented number of simultaneous microwave observations into the profile retrieval problem. Combining both remote sensing and *in situ* observations through the optimal estimation framework enables identification of the differences between observed and modeled brightness temperatures and radar reflectivities. These differences represent the best knowledge of the inherent uncertainties in forward modeling ability due to the underlying assumptions.

This dissertation will describe an optimal estimation algorithm that integrates three sets of airborne radar observations, seven microwave radiometer channels, and *in situ* cloud probe particle measurements to provide enough data to constrain the retrieval of an ice cloud and retrieve all three parameters of a normalized gamma PSD: N_o^*, μ, and D_m.

Chapter two gives an overview of the Wakasa Bay experiment and details the observational data collected and used in the retrieval. Chapter three explains the details of the forward radiative transfer model used in the retrieval. Chapter four details optimal estimation theory and its application to the retrieval. Chapter five explains the theory and

application of information content analysis applied within an optimal estimation retrieval framework.

Chapter six explores the results of a radar-only, single-level retrieval at the flight level of the *in situ* instruments. The retrieval is validated against the *in situ* measurements and the differences between these are explored through a sensitivity analysis. Particle density and aspect ratio are selected as primary sources of uncertainty and optimal values are retrieved. The PSD retrieval is performed using the optimal density aspect ratio and again compared to the *in situ* measurements.

Chapter seven provides the results of the full vertical profile retrievals using the previously retrieved optimal density and aspect ratio and comparisons with the baseline model retrievals. The retrieval algorithm is validated against a clear sky scene and then applied to the full horizontal extent of the ice cloud. The information content of the retrieval is explored and a sensitivity analysis is performed.

Chapter eight is given to the discussion of both the single-level retrieval and its validation against the *in situ* measurements as well as the impact of the optimally retrieved density and aspect ratio as improved model assumptions. The improved model is compared to the default density and particle shape model for not only the single-level retrieval, but also the vertical profile retrieval. The vertical profiles are examined for physical understanding of the retrieved ice cloud. Finally, the uncertainty and information content of the retrievals are examined.

Chapter nine concludes the thesis with a look at both the single-level retrieval and in situ validation as well as the vertical profile retrieval, with and without improved

ssumptions and the broader implications of the results. The nature of the ice cloud retrieval and uncertainty is discussed and a recommendation for future work is given.

CHAPTER 2

WAKASA BAY EXPERIMENT

The Wakasa Bay field campaign was part of the Advanced Microwave Scanning Radiometer (AMSR) Rainfall validation effort. As part of the physical validation effort, the experiment in Wakasa Bay was designed to provide simultaneous observation of clouds and precipitation by a comprehensive suite of active and passive microwave remote sensors. Using a combination of 11 passive microwave frequencies from 10 to 340 GHz, a dual-frequency precipitation radar at 13.4 and 35.6 GHz and a cloud radar at 94.9 GHz, as well as simultaneous *in situ* data, the Wakasa Bay data set represents our best ability to constrain the microwave inverse problem.

The AMSR-E Precipitation Validation Experiment was a joint United States/Japanese experiment to validate the precipitation retrievals from the Advanced Microwave Scanning Radiometer, a Japanese contribution to the Aqua satellite. The National Aeronautics and Space Administration (NASA) contribution to the experiment was the NASA P-3 aircraft with an instrument payload directed towards the sensing of solid and liquid precipitation. The P-3 was based at Yakota AFB (near Tokyo) and was dedicated to this experiment for most of January and early February 2003. The Japanese AMSR validation team contributed a Gulfstream II aircraft with microwave radiometers and an *in situ* cloud physics payload, two ground-based C-band Dual Polarized Doppler

radars (at Unami and Mikuni) and a large assortment of ground- and ship-based *in situ* sensors. United States and Japanese scientists planned the individual flight missions jointly. The goals of the AMSR-E precipitation team are summarized in Table 2.1.

Table 2.1. Goals of the AMSR-E precipitation team for the Wakasa Bay experiment.

1. To determine length scales of mid-latitude precipitation for beam-filling corrections.
2. To validate freezing level retrievals.
3. To investigate radiative transfer in bright bands associated with stratiform precipitation.
4. To test algorithms for the retrieval of snowfall over the ocean.
5. To test models for computing radiative transfer in precipitation.
6. To gather data for the development of retrieval algorithms for rain and snow fall over land.
7. To test algorithms for the retrieval of Cloud Liquid Water Content.
8. To determine the variability of the surface emissivity at frequencies relevant to precipitation retrievals
9. To test methods for measuring the rain drop size distribution remotely.
10. To obtain data for meteorological case studies.

In order to achieve the goals presented in Table 2.1, an extensive payload was installed in the P-3 including:

1. Polarimetric Scanning Radiometer (PSR): a multi-frequency radiometer with flexible scan patterns to simulate the AMSR-E and other measurement geometries. The PSR has channels at 10.7, 18.7, 21.5, 37, and 89 GHz (Piepmeier and Gasiewski, 1996).
2. Millimeter-wave Imaging Radiometer (MIR): cross-track, scanning radiometer with channels at 89, 150, 220, and 340 GHz and three channels near 183.3 GHz (Racette et al., 1996).

3. Airborne second generation Precipitation Radar (APR-2): a cross-track, scanning, Doppler radar with two frequencies at 13.405 and 35.605 GHz (Sadowy et al., 2003).
4. Airborne Cloud Radar (ACR): a 94.9 GHz nadir-viewing (non-scanning) cloud and precipitation radar (Sadowy et al., 1997).

The data collected on these flights, summarized in Table 2.2, addressed all of the defined objectives. Rainfall of various intensities with freezing levels from about 3 km all the way down to the surface and snowfall intensity varying from very light to very heavy was observed over ocean. In many cases, satellite coverage from AMSR-E and TRMM complements the airborne and surface-based observations. More detail on the sensors and how to obtain the data can be found at: http://nsidc.org/data/amsr_validation/rainfall/.

Table 2.2. Summary of P-3 Flights in Wakasa Bay Experiment.

Flight Date	Comments
Jan. 14, 2003	Sea of Japan, Rain/snow, low freezing levels
Jan. 15, 2003	Snow and a little rain over land (Northern Honshu)
Jan. 19, 2003	Oceanic rain, frontal crossing
Jan. 21, 2003	Oceanic rain
Jan. 23, 2003	Intense oceanic rain over Pacific
Jan. 26, 2003	Short flight over ground truth site at Fukui
Jan. 27, 2003	Joint with G-II, Sea of Japan, rain. Heavy rain over land on return
Jan. 28, 2003	Joint with G-II, Sea of Japan, snow, rain, snow over land
Jan. 29, 2003	Joint with G-II, Sea of Japan, snow over ocean and land
Jan. 30, 2003	Joint with G-II, Sea of Japan, snow over ocean and land
Feb. 1, 2003	Short flight over ground truth site at Fukui
Feb. 3, 2003	Scattered rain cells over Pacific Ocean

Dr. Masataka Murakami of the Japanese Meteorological Research Institute provided data from the Gulfstream (G-II) aircraft flown as part of the Japanese contribution to the Wakasa Bay experiment. Among the instruments flown on the

Japanese G-II aircraft were two-dimensional cloud (2DC) and two-dimensional precipitation (2DP) particle measuring probes. These instruments image particles that pass into the probe and record the size of the particles. The processed 2DC and 2DP data include the flight information (position, altitude, temperature, pressure, etc.), sample volume for each sample period, and particle concentrations per particle diameter bin.

The criteria for selecting a flight line for study was that it had both P-3 and G-II data and that the PSR instrument was scanning in cross-track mode such that nadir pointing data could be obtained from all instruments. After reviewing flights meeting those criteria, a leg of the 27 January data was selected. This flight leg offered a mix of rain, ice, cloud and clear air scenes and was thus well suited for testing the observations and forward model under a variety of conditions. Figure 2.1 shows the synchronized remote sensing data over the flight line selected for study.

To facilitate the use of observations from sensors with different sampling rates and spatial resolution, each instrument's data was processed into a common grid. In preparing the flight line, the raw data from each sensor were first synchronized by time. Only nadir-pointing data were used for ease of comparison between instruments. The radar data were filtered to remove ground clutter and then all data were interpolated into a common spatial grid oriented along the direction of flight with 1 km horizontal spacing and 150 m vertical spacing. Figure 2.2 shows the gridded remote sensing data over the flight line.

The stated uncertainties in the radars are +/– 1 dB at 10-km range for the APR-2 and +/- 1 dB for the ACR. The stated sensitivity threshold for each radar at 6 km is 5 dB for the APR-2 and –38 dBZ for the ACR. For the ice cloud retrieval performed here, the

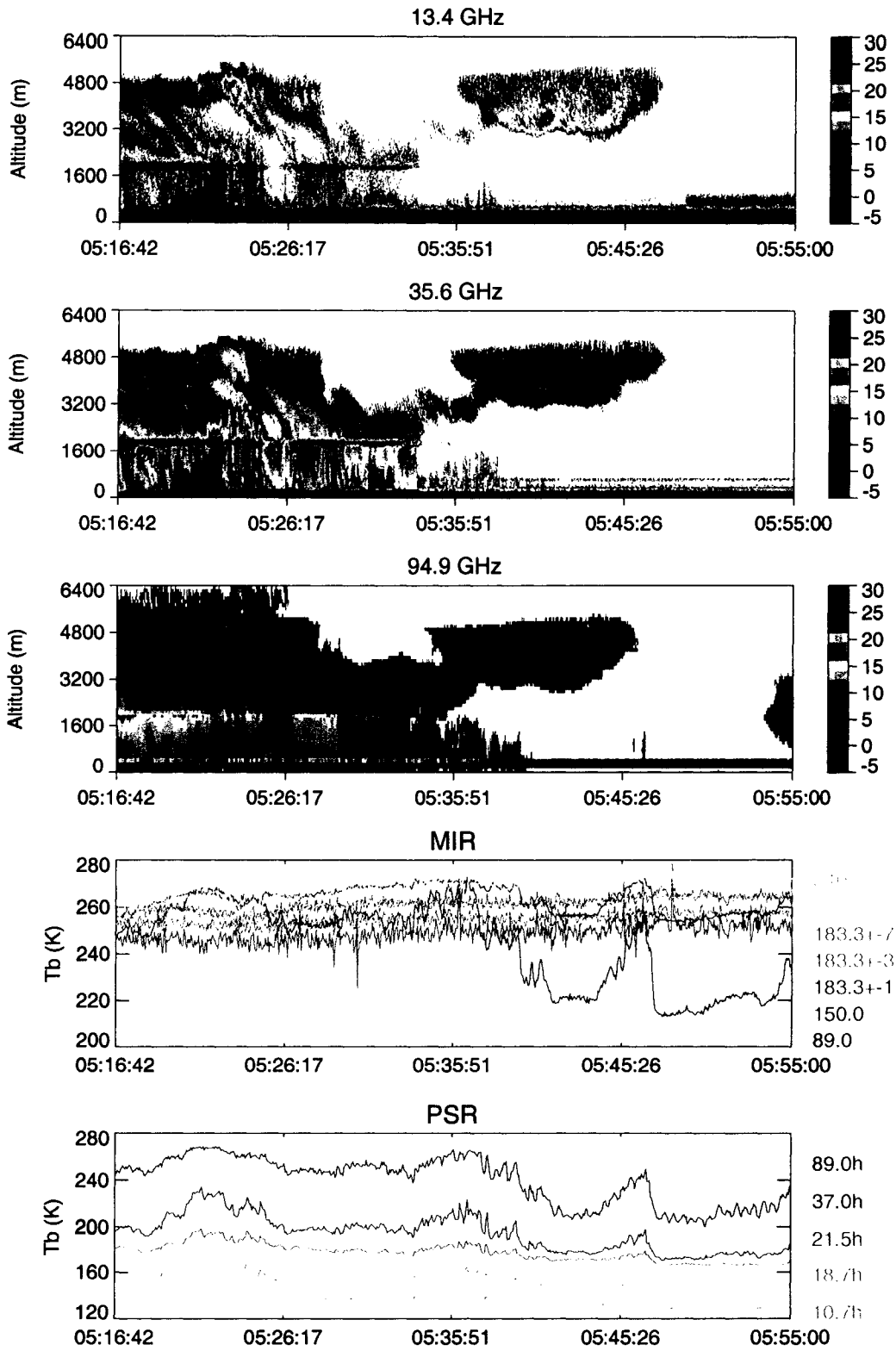

Figure 2.1. Ungridded flight line from 27 Jan 2003. The radar color bar is in dBZ.

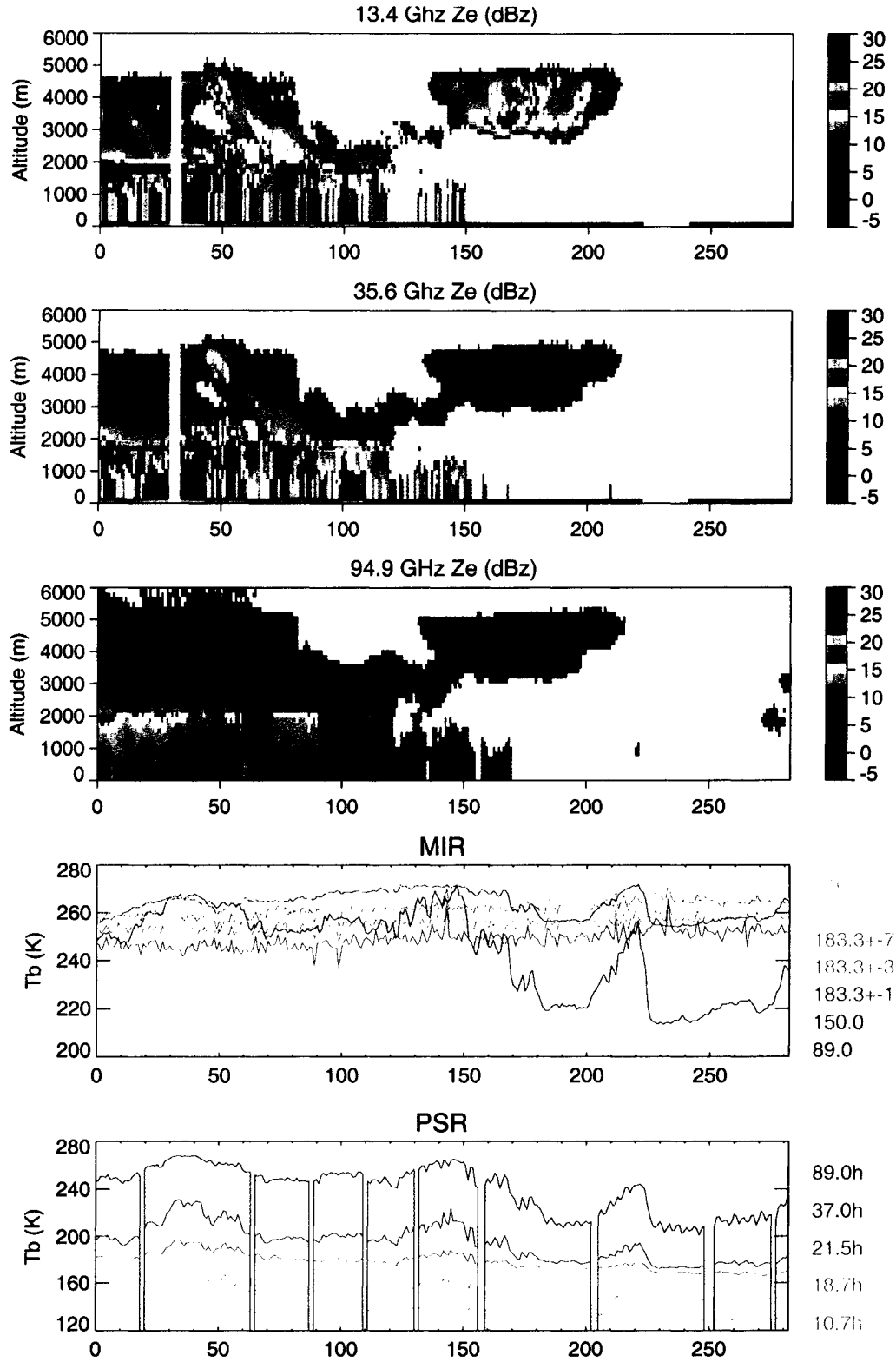

Figure 2.2. Gridded flight line from 27 Jan 2003. The horizontal grid spacing is 1 km and the vertical grid spacing is 150 m. The radar color bar is in dBZ.

reflectivities are close to the sensitivity threshold of the APR-2 instrument. When operating in this range, the APR-2 can suffer from quantization resulting in a nonlinear uncertainty, which increases as the observed reflectivities get closer to the threshold.

Note that the gridded data in Figure 2.2 shows data dropouts that did not appear in the raw data in Figure 2.1. The raw data files were plotted in consecutive scan order synchronized by start and end times without regard to any missing data. Therefore, once the raw data were gridded and processed, any time gaps in the data will now appear, as evident in Figure 2.2.

The *in situ* data were matched against the selected P-3 flight line and interpolated into the same horizontal grid as the remote sensing data. The G-II aircraft only offered data at a single altitude for the ice cloud under investigation and the aircraft altitude was used to place the *in situ* data into the corresponding vertical grid box. Note that the spatially collocated *in situ* data are not concurrent in time with the remote sensing data. There is a time lag (P-3 – G-II) of 317 to 348 seconds for each grid in the scene.

In modeling the size distribution of particles using the 2DP and 2DC probes, the 2DC probes have greater accuracy below 1000 μm and the 2DP probes have greater accuracy above 1000 μm. Heymsfield et al. (2002) state, for 2DC to 2DP PSD combinations, it is appropriate to use the 2DC up to 1000 μm and the 2DP for particles larger than 1000 μm. Additionally, they note that 2DC probe counts are typically underestimated below 100 μm. Therefore, the particle size distribution for any point is a combination of the 2DC and 2DP data with a step from 2DC to 2DP at 1000 μm. However, there is a significant discrepancy between the PSD measured by the two instruments as seen in Figure 2.3. The 2DC instrument counts 3-100 times the number

concentration of the 2DP instrument for any size bin in the ungridded data. Figure 2.4 shows the discrepancy of nearly a factor of 10 between the two instruments at the 1000 μm size bin. The 1000 μm bin is where the transition from one instrument to the other takes place for building a combined 2DC - 2DP PSD. The impact of this uncertainty in PSD is discussed in the sensitivity analysis section.

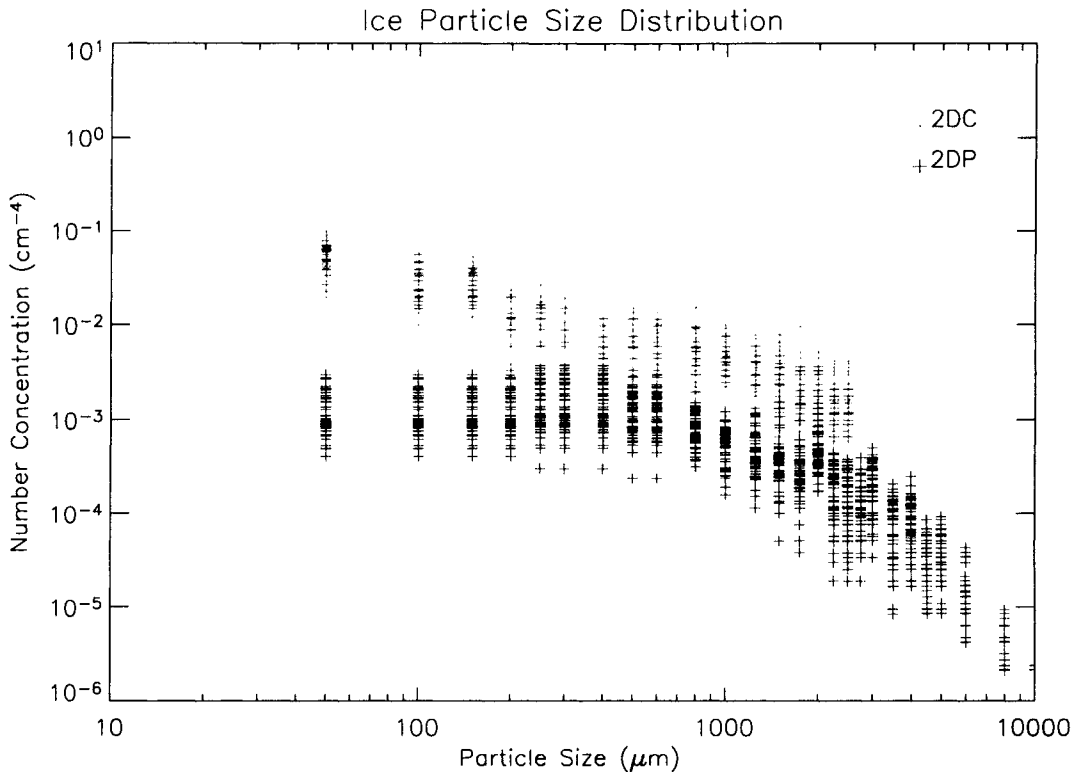

Figure 2.3. *In situ* ice cloud particle size distribution as measured by 2DC and 2DP probes. The PSD shown is a combination of 2DC and 2DP probes: 2DC probe below 1000 μm and 2DP probe above 1000 μm. The plot represents the PSD across the horizontal extent of the cloud from grid point 150-205.

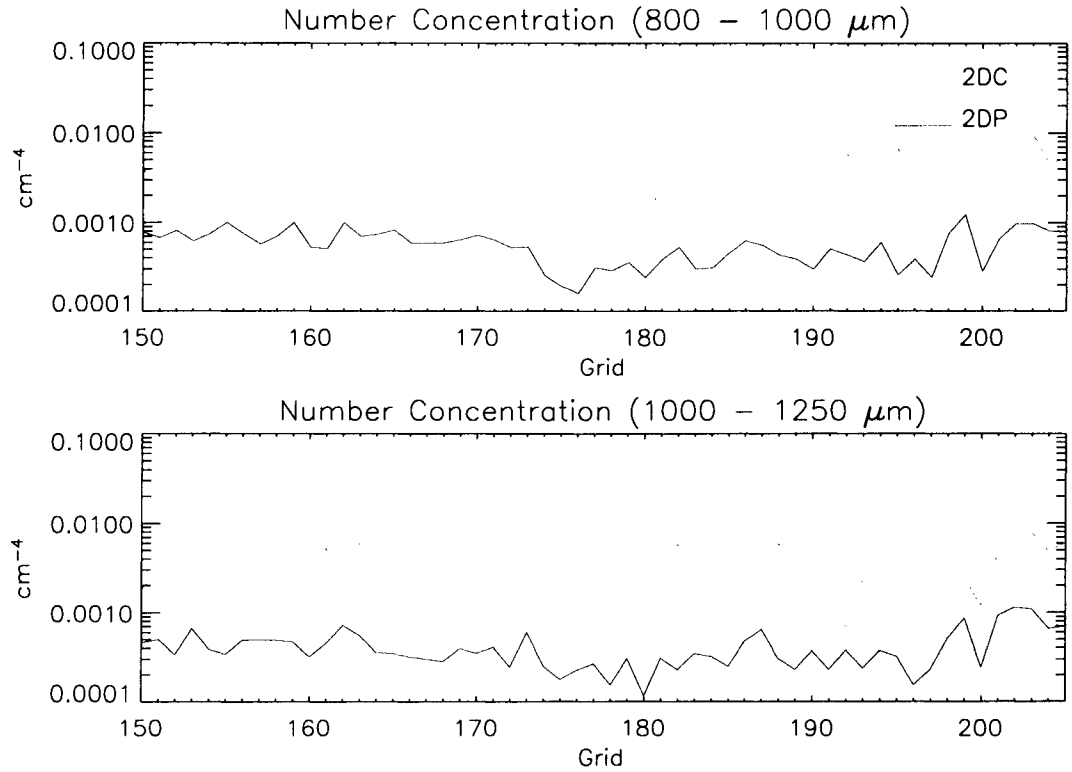

Figure 2.4. The *in situ* PSD number concentration around 1000 μm. The top plot shows the number concentration for each grid point across the cloud in the size bin from 800 –1000 μm and the bottom plot shows the number concentration in the size bin from 1000–1250 μm.

CHAPTER 3

FORWARD RADIATIVE TRANSFER MODEL

Observed microwave radiances at the top of the atmosphere originate partly at the surface and partly from the atmosphere. Radar reflectivities are solely the result of scattering and absorbing constituents in the atmosphere. The surface contribution to microwave radiances depends both on the nature of the surface and its temperature. The atmospheric contribution to microwave radiances comes from constituents such as oxygen, water vapor and cloud water both absorbing and emitting upwelling radiation. Liquid precipitation drops absorb and scatter and cloud ice also acts to scatter upwelling radiation. A full model of the radiative transfer through the atmosphere must include the surface emission plus atmospheric emission and multiple scattering terms. The emissivity, ε, of the ocean surface typically ranges between 0.4 and 0.6 and depends on surface roughness, salinity and sea foam (Liou, 2002). The surface roughness for an ocean surface is typically related to wind-driven waves and thus to near-surface wind speed. An ocean surface emissivity model based on Wilheit (1979) is used to compute emissivity as a function of wind speed and surface temperature.

Atmospheric absorbers of microwave radiation include water vapor, molecular oxygen and cloud water. Water vapor and molecular oxygen provide the background

atmospheric absorption. A representative pressure profile is used in this study to provide the oxygen information. A column value for relative humidity and lapse rate yield the background water vapor. Cloud water and ice are treated separately from this background absorption and emission as part of a particle size distribution of hydrometeors.

The absorbing and scattering characteristics (extinction coefficient k, single scatter albedo a, and the phase function $P(\Theta)$) of the hydrometeors in the cloud volume are calculated using Rayleigh, Mie and T-matrix theory. For a given size, temperature, particle density and frequency of radiation, the complex index of refraction of the media is calculated using Maxwell-Garnett mixing theory (Maxwell-Garnett, 1904) as generalized by Bohren and Battan (1982). Given the complex index of refraction and the size parameter ($\chi = \pi * D/\lambda$) of the particle, the scattering and absorbing characteristics can be calculated. For smaller particles, the Rayleigh approximation may be made. However, as particles get larger and approach a size parameter $\chi \sim 1$, the Rayleigh approximation is no longer valid. Note that the failure of the Rayleigh condition depends on both the frequency of the incident wave and the index of refraction of the scattering media. From Ulaby (1981), the Rayleigh approximation may be applied where $|n| * \chi < 0.5$. Here n is the refractive index of the particle (the real part of the complex index of refraction). For particles larger than this condition, Mie theory is used to calculate the scattering and absorption properties of the hydrometeors.

Because cloud ice particles are typically aspherical, the forward model needs to account for these particles as well. A T-matrix method was used to calculate the scattering by nonspherical particles. The T-matrix code was obtained from Barber and Hill (1990) for axi-symmetric oblate spheroids. Supplied with the size parameter of the

particle (D = semi-major axis of spheroid), the axis ratio of the spheroid and the orientation of the incident wave, the T-matrix code calculates the scattering characteristics for a nonspherical particle.

The T-matrix nonspherical ice particles are oblate spheroids. These oblate spheroids are preferentially oriented with their semi-major axis perpendicular to the vertical. The cloud probe instruments return a PSD using the maximum dimension of the imaged particle. This maximum dimension is assumed to be the length of the semi-major axis of the T-matrix oblate spheroid. Thus the volume of an oblate spheroid with semi-major axis = D and minor axis = $D*{}^{a}/_{b}$ is less than the volume of a sphere with diameter = D.

In the case of forward modeling *in situ* measurements of PSD, the model operates explicitly on the measured number concentrations as a function of particle diameter. The density of the ice particles is prescribed to yield the bulk ice mass characteristics. However, a single constant density would be inappropriate as snow density decreases with particle size (Heymsfield et al., 2004). The individual ice particle density-size relationship from Brown and Francis (1995) is used to calculate the density as a function of particle diameter (D) across the PSD,

$$\rho({}^{g}/_{cm^3}) \approx 0.07D^{-1.1} \tag{3.1}$$

for $D > 0.1$ mm. Units of D are mm.

When an explicit *in situ* PSD is not present (i.e., for a retrieval of PSD parameters) the model uses a normalized gamma distribution (Testud et al., 2001) to represent the PSD. The normalized gamma distribution has several advantages over a typical gamma PSD. A typical gamma PSD would be of the form

$$N(D) = N_o D^{\mu} e^{-\Lambda D}, \tag{3.2}$$

where $N(D)$ is the number concentration as a function of particle diameter D, N_o is the intercept, μ is the order or shape of the gamma function and Λ is the slope of the distribution. Here N_o and λ represent a mixture of the liquid water content (LWC), D_m and the shape. This formulation proves problematic in PSD retrievals. N_o's dimension itself ($m^{-4-\mu}$) is ill defined and N_o can be affected by variation correlated with variation in μ (Testud et al., 2001). This variation on N_o with μ requires *a priori* restrictions on the variance in μ in order to enable retrieval convergence (Benedetti et al., 2003).

The normalized gamma distribution is of the form

$$N(D) = N_o^* F_{\mu}(\frac{D}{D_m}), \tag{3.3}$$

where D_m is the mean volume diameter as defined by the fourth moment of the PSD divided by the third moment,

$$D_m = \frac{\int_0^{\infty} N(D) D^4 dD}{\int_0^{\infty} N(D) D^3 dD}. \tag{3.4}$$

N_o^* is the normalized intercept

$$N_o^* = N_o D_m^{\mu} \frac{\Gamma(4+\mu)}{\Gamma(4)} \frac{4^4}{(4+\mu)^{4+\mu}}, \tag{3.5}$$

and $F_{\mu}(x)$ is the normalized shape of the PSD,

$$F_{\mu}(x) = \frac{\Gamma(4)}{4^4} \frac{(4+\mu)^{4+\mu}}{\Gamma(4+\mu)} x^{\mu} \exp[-(4+\mu)x]. \tag{3.6}$$

The advantages of the normalized PSD are first that the three PSD parameters now have physical meaning: D_m represents a characteristic particle size, N_o^* is the

intercept parameter of an exponential distribution of the same LWC and D_m, and μ is the shape of the PSD. Further, this normalization eliminates the strong variation in N_o with μ without any *a priori* assumption on the shape of the PSD. This will prove essential to the retrieval of PSD parameters.

Once the radiative properties of the surface and atmosphere are known, one can apply radiative transfer techniques to compute the brightness temperatures or backscattered radiation reaching the sensor. The forward radiative transfer model uses a two-stream unscaled Eddington approximation for plane-parallel calculations. All retrievals are made at nadir incidence and over water. Kummerow (1993) gives the details of the Eddington approximation and shows it to be accurate to within 6 K for a single uniform hydrometeor layer, within 3 K for more realistic multi-layered cloud hydrometeor profiles and within 0.2 K in the absence of scattering constituents over the range of frequencies from 6.6 – 183 GHz. Smith et al. (2002) showed the two-stream Eddington approximation to normally be accurate within 1 K at nadir incidence over ocean when compared to more complex 16-stream and Monte Carlo models. Roberti et al. (1994) compared an Eddington plane-parallel code against 3-D Monte Carlo and discrete ordinates methods at nadir incidence. They find that at lower emission-dominated frequencies, errors introduced by the plane-parallel code are quite small. For frequencies where scattering dominates (89 GHz and higher), the differences between plane-parallel and more accurate 3-D methods can be significant and up to 8 K for high ice content clouds (IWC = 5 gm^{-3}) at 85.6 GHz and are an increasing function of frequency (size parameter).

The ice cloud under study has an ice water content of 1.0×10^{-3} to 1.0×10^{-4} gm^{-3}. This range of ice water contents is far less than that in either the Roberti or Smith studies and the characteristic size parameters of the particles should be much less as well. The characteristic uncertainty in brightness temperatures due to scattering should consequently be less than either Roberti or Smith found.

CHAPTER 4

OPTIMAL ESTIMATION METHODOLOGY

Atmospheric remote sensing involves the interpretation and inversion of radiometric measurements, where the measured radiation is characterized by a specific wavelength that is sensitive to some physical aspect of the medium (Liou, 2002). The propagation of radiation through a medium is described by a radiative transfer model:

$$\mathbf{y} = \mathbf{f}(\mathbf{x}) \tag{4.1}$$

where $\mathbf{y}$ is a vector of dimension m representing the radiometric measurements or observations, $\mathbf{x}$ is a vector of dimension n representing the state or physical aspects of the medium through which the radiation has traveled and $\mathbf{f}$ is the forward function that maps from state space to measurement space (Rodgers, 2000).

In this formulation, there is a single ideal measurement vector $\mathbf{y}$ corresponding to the state vector $\mathbf{x}$ and determined by the physics of the measurement contained in $\mathbf{f}(\mathbf{x})$. However, in practice, not only is there always measurement error, but also it is often necessary to approximate the exact physics of the forward function by a forward model $\mathbf{F}(\mathbf{x})$.

Thus, our relationship between observation vector and state vector becomes

$$\mathbf{y} = \mathbf{F}(\mathbf{x}) + \boldsymbol{\varepsilon}, \tag{4.2}$$

where $\mathbf{y}$ is the measurement with uncertainty $\boldsymbol{\varepsilon}$ and $\mathbf{F(x)}$ is a vector-valued function of the state that contains our understanding of the physics. Note that $\mathbf{F(x)}$ is a model with its own inherent uncertainty due to approximations of the underlying physics. These approximations are required either due to a lack of knowledge of the physical processes being modeled or in the interests of computational efficiency.

Now, consider a linearization of the forward model about some reference state $\mathbf{x_0}$,

$$\mathbf{y} - \mathbf{F}(\mathbf{x}_0) = \frac{d\mathbf{F}(\mathbf{x})}{d\mathbf{x}} * (\mathbf{x} - \mathbf{x}_0) + \boldsymbol{\varepsilon} = \mathbf{K} * (\mathbf{x} - \mathbf{x}_0) + \boldsymbol{\varepsilon}, \tag{4.3}$$

where $\mathbf{K}$ is the m x n weighting function matrix with elements

$$\mathbf{K}_{ij} = \frac{\partial \mathbf{F}_i(\mathbf{x})}{\partial \mathbf{x}_j}. \tag{4.4}$$

$\mathbf{K}$ is also known as the Jacobian or kernel.

If the measurement space is modeled having dimension m and state space has dimension n, then the act of measurement is equivalent to mapping from state space to measurement space. $\mathbf{K}$ then represents that forward mapping while $\mathbf{K}^{-1}$ represents the inverse, going from measurement space to state space.

For a linear problem, in the absence of measurement error or uncertainty, the inverse problem reduces to the exact solution of the set of linear equations

$$\mathbf{y} = \mathbf{K}\mathbf{x}. \tag{4.5}$$

However, all real measurements are subject to some experimental error or noise. One way to describe the uncertainty around a measurement is to use a probability density function in a Bayesian approach to probability.

The statement that a scalar measurement has a value $\bar{y}$ and error σ is a way of saying our knowledge of the true value of the measured parameter is described by a probability density function (PDF) $P(y)$ with a mean value $\bar{y}$ and variance σ^2 where

$$\bar{y} = \int yP(y)dy \tag{4.6}$$

and

$$\sigma^2 = \int (y-\bar{y})^2 P(y)dy. \tag{4.7}$$

Here the probability that y lies in the interval $(y, y + dy)$ is $P(y)dy$ and that probability is a measure of knowledge about y. The form of $P(y)$ is often taken to be Gaussian:

$$P(y) = \frac{1}{2\pi^{\frac{1}{2}} * \sigma} \exp\{-\frac{(y-y)^2}{2\sigma^2}\}. \tag{4.8}$$

When the measured quantity is a vector, a probability density can still be defined over measurement space with the interpretation that $\mathbf{P(y)}d\mathbf{y}$ is the probability that the true value of the measurement lies in the multidimensional interval $(\mathbf{y}, \mathbf{y} + d\mathbf{y})$ in measurement space. Different elements of a vector may be correlated

$$\mathbf{S}_{ij} = <(\mathbf{y}_i - \bar{\mathbf{y}}_i)(\mathbf{y}_j - \bar{\mathbf{y}}_j)> \neq 0, \tag{4.9}$$

where $\mathbf{S}_{ij}$ is the covariance and $< >$ is the expectation value operator. $\mathbf{S}$ is the matrix consisting of all $\mathbf{S}_{ij}$ and the diagonal of $\mathbf{S}$ consists of the variances, σ^2, of individual elements of $\mathbf{y}$.

The Gaussian PDF of a vector is then

$$\mathbf{P(y)} = \frac{1}{(2\pi)^{\frac{m}{2}} |\mathbf{S}_y|^{\frac{1}{2}}} \exp\{-\frac{1}{2}(\mathbf{y}-\bar{\mathbf{y}})^T \mathbf{S}_y^{-1} (\mathbf{y}-\bar{\mathbf{y}})\}. \tag{4.10}$$

Now that the measurement is written in terms of a PDF, how then does the inverse model relate the state to the measurement? The act of measurement maps the state into

measurement space according to the forward model. However, the measurement error ε is known only statistically so that a point in state space maps into a region in measurement space given by the PDF of ε.

There may also be some other prior information about the state, such as climatology, which can be described by a PDF. This additional information can be used to constrain the solution. Given a prior state PDF, Bayes theorem provides a way to update the prior knowledge or expectation about the state in light of new information from the measurement.

$P(x)$ is defined as the prior PDF of the state x describing the probability before the measurement that x lies in $(x, x + dx)$. $P(y)$ is the prior PDF of the measurement y. $P(x,y)$ is the joint prior PDF of x and y describing the probability that x is in $(x, x + dx)$ and y is in $(y, y + dy)$. $P(y|x)$ is the conditional PDF of y given x, i.e., the knowledge of y that would be obtained if the state were x. It can be explicitly determined from the forward model and the statistical description of the measurement error. $P(x|y)$ is the conditional PDF of x given y and is the quantity of interest in the retrieval.

Bayes theorem can be written as

$$P(x \mid y) = P(y \mid x) * \frac{P(x)}{P(y)} \tag{4.11}$$

or the posterior PDF of the state x when the measurement y is given. This theorem provides a conceptual approach to the inverse problem when the quantities of interest and their uncertainties are described in statistical terms. Before any measurement, *a priori* knowledge of the state is expressed as a prior PDF. Next, the measurement process is described as a forward model mapping from state space to measurement space. Finally,

Bayes Theorem provides a formalism for inverting the mapping function to calculate a posterior PDF by updating the prior with new information from the measurement.

The simplest case to illustrate this process is a problem with a linear forward model and Gaussian PDFs:

$$\mathbf{y} = \mathbf{F}(\mathbf{x}) + \boldsymbol{\varepsilon} = \mathbf{K} * \mathbf{x} + \boldsymbol{\varepsilon}. \tag{4.12}$$

Now write the posterior PDF in Gaussian format,

$$-2\ln\mathbf{P}(\mathbf{x} \mid \mathbf{y}) = (\mathbf{x} - \hat{\mathbf{x}})^T * \mathbf{S}_x^{-1} * (\mathbf{x} - \hat{\mathbf{x}}) + c, \tag{4.13}$$

and substitute into Bayes Theorem to solve for $\hat{\mathbf{x}}$,

$$\hat{\mathbf{x}} = \mathbf{x}_a + (\mathbf{K}^T\mathbf{S}_y^{-1}\mathbf{K} + \mathbf{S}_a^{-1})^{-1} * \mathbf{K}^T\mathbf{S}_y^{-1} * (\mathbf{y} - \mathbf{K}\mathbf{x}_a), \tag{4.14}$$

where $\hat{\mathbf{x}}$ is the expectation or mean value for the state and $\mathbf{S}_x$ is the associated error covariance matrix,

$$\mathbf{S}_x = (\mathbf{K}^T\mathbf{S}_y^{-1}\mathbf{K} + \mathbf{S}_a^{-1})^{-1}. \tag{4.15}$$

Thus, the class of possible states consistent with the available information has been identified with its associated PDF. Typically, however, the desired solution is a single state accompanied by an estimate of uncertainty. Thus an objective method to select one state from the PDF is required.

A common approach is to use the posterior PDF of the state vector and represent the solution as the most likely state with the error covariance as the uncertainty. This approach is called the maximum *a posteriori* (MAP) solution. Maximizing the posterior PDF produces $\hat{\mathbf{x}}$ as the most probable state and $\mathbf{S}_x$ as the corresponding uncertainty. Another approach is to minimize the variance, corresponding to least squares in the scalar case. In the case of Gaussian PDFs, these two approaches are equivalent.

This analytical solution is applicable for the consideration of linear problems. However, the radiative transfer problem is nonlinear. For moderately nonlinear problems, since no general explicit expression can be found for locating an optimal solution, they must be found numerically and iteratively using a Gauss-Newton method:

$$\mathbf{x}_{i+1} = \mathbf{x}_i + (\mathbf{S}_a^{-1} + \mathbf{K}^T\mathbf{S}_y^{-1}\mathbf{K}_i)^{-1} * [\mathbf{K}_i^T\mathbf{S}_y^{-1}(\mathbf{y} - \mathbf{F}(\mathbf{x}_i)) - \mathbf{S}_a^{-1}(\mathbf{x}_i - \mathbf{x}_a)]. \quad (4.16)$$

The iteration stops when a convergence criterion is satisfied,

$$(\mathbf{x}_i - \mathbf{x}_{i+1})^T\mathbf{S}_x^{-1}(\mathbf{x}_i - \mathbf{x}_{i+1}) << n \quad (4.17)$$

where n is the number of degrees of freedom in the problem. This criterion is satisfied when the difference between iterative steps is less than the uncertainty of the retrieved state. The convergence or non-convergence of the retrieval is a first level diagnostic to the validity of the inverse problem. An ill-posed problem will have a difficult time reaching convergence with realistic input covariance. In addition to the convergence criterion, there is a set of readily available diagnostic tools to evaluate the quality of the retrieval.

The most obvious diagnostic tool is the retrieval covariance matrix $\mathbf{S}_x$. Combined with the expectation (mean in our Gaussian case) state $\hat{\mathbf{x}}$, $\mathbf{S}_x$ describes the distribution of possible retrieved states. The width of this PDF can be interpreted as the uncertainty around the retrieved state. The diagonal elements of $\mathbf{S}_x$ are the variances for each retrieved parameter while the off-diagonal elements indicate correlations in uncertainties between retrieved parameters.

The next diagnostic tool is the *a priori* matrix defined as

$$\mathbf{A} = \mathbf{S}_x\mathbf{K}_1^T\mathbf{S}_y^{-1}\mathbf{K}_1. \quad (4.18)$$

A is the sensitivity of the retrieval to the true state, while ($\mathbf{I}_n$ - **A**) is the sensitivity of the retrieval to the *a priori* (Rodgers, 2000). In an ideal inverse problem, **A** would be a unit matrix, indicating that the retrieval is based exclusively on the measurements. Any deviation away from unity for the diagonal elements of **A** indicates the contribution of the *a priori* to the retrieved state.

A χ^2 test can be applied to determine if the retrieval vector belongs to the assumed Gaussian distribution. χ^2 tests what fraction of members of the Gaussian distribution has a probability density less than that of the vector being tested (Rodgers, 2000).

$$\chi^2 = (\mathbf{F}(\mathbf{x}) - \mathbf{y})^T \mathbf{S}_y^{-1} (\mathbf{F}(\mathbf{x}) - \mathbf{y}) + (\mathbf{x} - \mathbf{x}_a)^T \mathbf{S}_a^{-1} (\mathbf{x} - \mathbf{x}_a) \qquad (4.19)$$

compares the difference vector ($\mathbf{F}(\mathbf{x}) - \mathbf{y}$) to a Gaussian distribution with zero mean and covariance $\mathbf{S}_y$ and likewise the vector ($\mathbf{x}$ - $\mathbf{x}_a$) to a distribution with zero mean and covariance $\mathbf{S}_a$. χ^2 should be approximately equal to the number of independent parameters, *n*, in the retrieval. If χ^2 varies much from *n*, then either the retrieved vector or the Gaussian distributions (covariance) may be suspect. If χ^2 is much greater than *n*, then the retrieval vector is an outlier and this can indicate that the input covariance may be underestimated, and thus the retrieved covariance would also be underestimated. If χ^2 is much less than *n*, the input covariance may be overestimated and the retrieval covariance would be correspondingly too large.

Because the input covariance impacts not only the final retrieved state distribution but also whether the retrieval can converge at all, proper estimation of the input covariances is essential. However, there are few universally accepted methodologies for estimating the error covariance matrices. The *a priori* error covariance matrix, $\mathbf{S}_a$, is

relatively straightforward. The *a priori* matrix should represent the knowledge of all possible states before the measurement. If the *a priori* knowledge of a state is derived from a source like climatology, then the climatology can be modeled as a PDF with a most likely value and a variance. Providing a representative *a priori* PDF for each parameter in the state vector produces a diagonal *a priori* covariance matrix.

Performing a similar process for each parameter in the measurement vector can also provide a measurement covariance matrix, $\mathbf{S}_y$. However, the $\mathbf{S}_y$ matrix represents the uncertainty in the entire measurement process, not simply the measuring instrument's accuracy. The measurement process has an overall uncertainty due to the accuracy and resolution of the sensor, but the principal contribution to overall $\mathbf{S}_y$ is due to uncertainties in the physical model used to map from measurement space into state space. Physical limitations and assumptions in the forward model contribute to uncertainty in the measurement.

These model uncertainties are more difficult to assess and thus include in $\mathbf{S}_y$. There are two principal approaches. The first approach is to test the sensitivity of the retrieval to changes in the underlying assumptions. In the linear case this can provide an estimate of the uncertainty due to the assumptions. In nonlinear cases, the sensitivity may vary greatly depending on the range of the assumed value and any indicated sensitivity may be accurate only around the immediate value tested. The second approach is to move the parameter in question from assumption to retrieval parameter. By retrieving the previously assumed parameter, one can treat the uncertainty around the unknown explicitly.

CHAPTER 5

INFORMATION CONTENT ANALYSIS

The optimal estimation methodology is particularly conducive to investigating the information content of both measurements and retrieval. Information content is a measure of how knowledge of the retrieval state is improved by the measurements. In the optimal estimation sense the knowledge of a state is described by a PDF defined by some most probable state or mean, and the variance around that state. The information content describes the degree to which the prior PDF (set of all possible states before the measurement) is reduced by the measurements. If the number of possible states is reduced from the prior PDF with a relatively large variance or distribution width to a posterior PDF with a smaller variance, then the measurements have added information. Information content can be defined qualitatively as the factor by which the uncertainty about a quantity is reduced by a measurement (Rodgers, 2000).

A common metric for the information content of a measurement (or set of measurements) is the Shannon information content (SIC) as described by Rodgers (2000). The SIC is an analog to thermodynamic entropy (S) which is the logarithm of the number of distinct internal states of a thermodynamic system consistent with its thermodynamic properties. The SIC is then the change in the logarithm of the number of distinct possible internal states of the system being measured, consistent with the change in knowledge of

the system resulting from a measurement (Rodgers, 2000). Therefore, consider a prior PDF, P_1, describing the probability of any given state occurring in a system. P_1 represents the *a priori* knowledge of a system before any measurements are made. If P_2 represents the probability distribution of states consistent with a measurement, then the difference in entropy between P_1 and P_2 defines the information content of the measurement:

$$H = S(P_1) - S(P_2). \tag{5.1}$$

If P_1 and P_2 are Gaussian PDFs with variance σ_1 and σ_2, then the entropy of P_1 may be written

$$S(P_1) = \frac{1}{2}\log_2 |\sigma_1| + c \tag{5.2}$$

where the constant $c = {}^{m}/_{2}\log_2(2\pi e)$ (L'Ecuyer et al., 2005). Then the SIC may be written

$$H = \frac{1}{2}\log_2 |\sigma_1\sigma_2^{-1}|. \tag{5.3}$$

Likewise, the optimal estimation definitions for the *a priori* and *a posteriori* PDFs is described by

$$H = \frac{1}{2}\log_2 |\mathbf{S_a}\mathbf{S_x}^{-1}|. \tag{5.4}$$

Thus the information content measures the reduction in uncertainty in state space from before the measurement ($\mathbf{S_a}$) to after the measurement ($\mathbf{S_x}$). In information theory it is convenient to use the base two logarithm so that the units of H are bits. H then represents the number of distinct states, 2^H, that can be distinguished from the prior state space by the measurements (L'Ecuyer et al., 2005).

H is a scalar comprised of matrices $\mathbf{S_a}$ and $\mathbf{S_x}$, which itself is a product of $\mathbf{S_a}$, $\mathbf{K}$, and $\mathbf{S_y}$. In this formulation, H measures the information content of the combination of all m components of the measurement vector $\mathbf{y}$. However, it can be insightful to examine the information content of a single component of $\mathbf{y}$, such as a single radiometer frequency brightness temperature, or a subset of $\mathbf{y}$ components, such as the set of returns from a single radar frequency comprising a vertical reflectivity profile. For a single element $\mathbf{y_i}$, $\mathbf{S_{xi}}$ will be written

$$\mathbf{S}_{xi} = (\mathbf{S}_a^{-1} + \mathbf{K}_i^T \mathbf{S}_{yi}^{-1} \mathbf{K}_i)^{-1}. \tag{5.5}$$

$\mathbf{S_{yi}}$ is a 1 x 1 matrix comprised of the variance for the single element $\mathbf{y_i}$. $\mathbf{K_i}$ is a 1 x n matrix corresponding to the ith row of $\mathbf{K}$. Thus, the product $\mathbf{K_i^T S_{yi}^{-1} K_i}$ has dimensions $(n \times 1) \cdot (1 \times 1) \cdot (1 \times n) = (n \times n)$, and so $\mathbf{S_{xi}}$ retains the same dimensionality as $\mathbf{S_x}$ but is comprised solely of the contributions from the ith element of $\mathbf{y}$. Using this H_y, the information content of each individual measurement or set of measurements can be calculated to assess which measurements contribute the most to the retrieval of each state parameter. The information content towards each retrieved parameter can also be broken out by the H for each element of $\mathbf{S_a}$ and $\mathbf{S_x}$ individually.

Another measure of the information content of a retrieval is the effective rank of the problem, or the number of independent measurements made to better than measurement error. From Rodgers (2000) the effective rank, N, of the problem is calculated as the number of singular vectors of $\mathbf{S_y^{-1/2} K S_a^{1/2}}$ that are greater than one. The effective rank can be interpreted as the number of independent quantities that can be retrieved from the measurements (L'Ecuyer et al., 2005).

A similar information metric is the degrees of freedom for signal, d_s, that represents the number of useful independent observations in a measurement. The quantity d_s can be written as

$$d_s = \frac{\mathbf{S}_i l_i^2}{1 + l_i^2} = tr(\mathbf{A}) \tag{5.6}$$

where l_i is a singular value of $\tilde{\mathbf{K}}$ and $\tilde{K}$ is the same quantity considered for N:

$$\tilde{\mathbf{K}} = \mathbf{S}_y^{-1/2} \mathbf{K} \mathbf{S}_a^{1/2}. \tag{5.7}$$

Note that d_s and N are analogous, but d_s applies in measurement space and N applies in retrieval (state) space.

Together, these information metrics provide a quantitative evaluation of the measurement and retrieval process. The degree of freedom for signal, d_s, tells if measurements are independent or redundant with respect to the retrieved state. Effective rank, N, can determine how many independent quantities can be retrieved from the measurements. The Shannon Information Content, H, provides a measure of how much information about the state has been added or how much uncertainty has been reduced by the measurements. H can also be broken into information contributions from individual measurements or instruments or information about individual parameters to see which instrument is most important to the retrieval and which parameter has the most information.

As can be seen from Equations (5.4), (5.5), and (5.7), all of the information content metrics depend on the *a priori* covariance $\mathbf{S_a}$. By defining the width of the prior distribution of states, $\mathbf{S_a}$ is a measure of the uncertainty in the knowledge of the retrieval state prior to the measurement. Since the information content is focused on the reduction

of uncertainty from pre- to post-measurement, an error in the estimate of $\mathbf{S_a}$ will be directly propagated through to the evaluation of the information content of a measurement or retrieval. If $\mathbf{S_a}$ is too large, H will be overestimated and vice-versa.

CHAPTER 6

SINGLE-LEVEL PSD RETRIEVAL

A retrieval of the PSD at a single vertical level was performed using the radar data from the APR-2 and ACR instruments at the flight level of the G-II aircraft to facilitate direct comparison with the 2DC probe measurements. The retrieval assumed a Brown and Francis (1995) size-density relationship for the particles in the ice cloud being retrieved. The particles were assumed to be spheres. The retrieved parameters were the three variables in the normalized gamma distribution, μ, N_o^*, and D_m, representing the cloud ice PSD. Emission and attenuation were ignored as the forward radiative transfer model considered only the scattering of the radar pulse from the single cloud volume at the layer coincident with the *in situ* measurements. Attenuation by ice in the range of the ice cloud under consideration is quite low, 0.2 dB/km at 94.9 GHz.

The retrieval obtained an optimal PSD for each individual grid point through the length of the cloud. The mean cloud retrieved normalized gamma PSD was $\mu = -1.12$, $N_o^* = 1.58 \times 10^7$ m^{-4}, $D_m = 2.2 \times 10^{-3}$ m. Because the cloud was relatively homogeneous at the flight level, a similar retrieval was performed that selected a single optimal gamma PSD for the entire cloud instead of for each individual grid point. The all-grid retrieved optimal PSD was $\mu = -1.77$, $N_o^* = 1.05 \times 10^7$ m^{-4}, $D_m = 2.2 \times 10^{-3}$ m. The single-grid cloud mean and all-grid retrieved normalized gamma PSDs for the entire flight line were

compared against the *in situ* measured PSD in Figure 6.1. The retrieved PSDs showed 10-100 times more particles per size bin then the *in situ* PSD. The ice water content (IWC) and D_m of the retrieved PSD were compared to the IWC and D_m of the *in situ* PSD in Figure 6.2. The retrieved PSD shows up to 10 times more IWC than the *in situ* and the retrieved particle mean volume diameters are much smaller than the *in situ*. These discrepancies are significant.

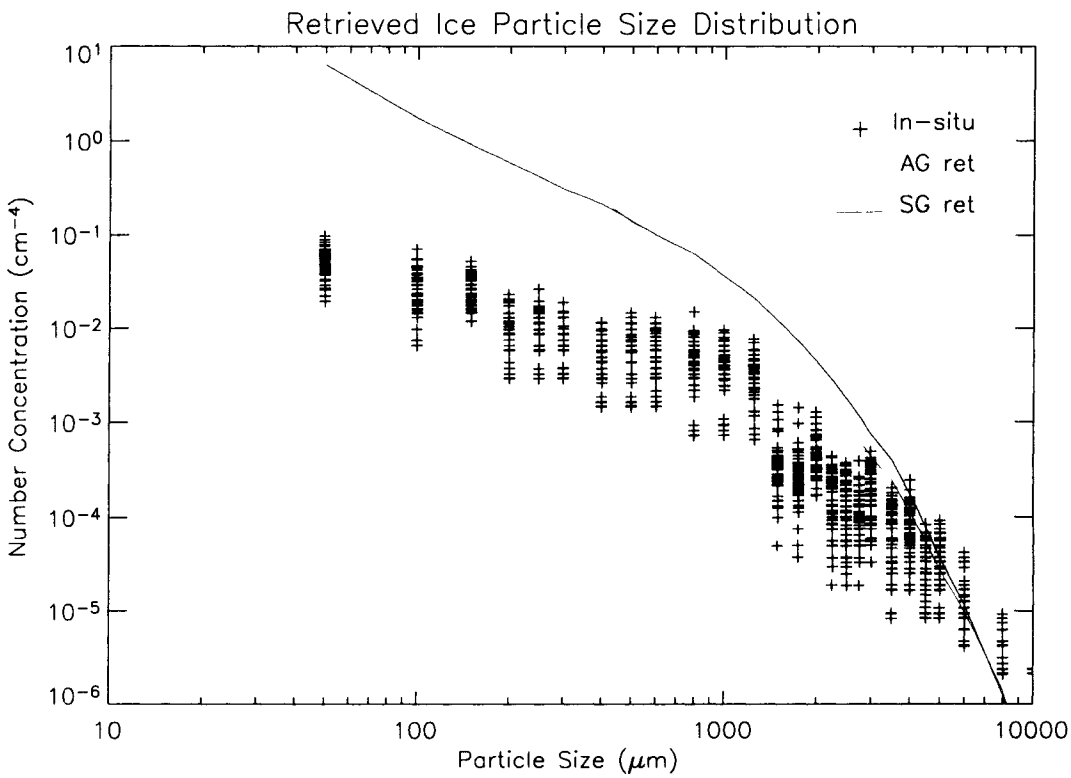

Figure 6.1. The retrieved PSD for the cloud using the default model assumptions of spherical particles and a Brown and Francis particle size-density relationship. The AG ret is the all-grid retrieval of a single optimal PSD for the entire cloud. The SG ret is the mean of single-grid retrievals of optimal PSDs for each gridpoint across the cloud. The retrieved PSDs are plotted over the *in situ* PSD.

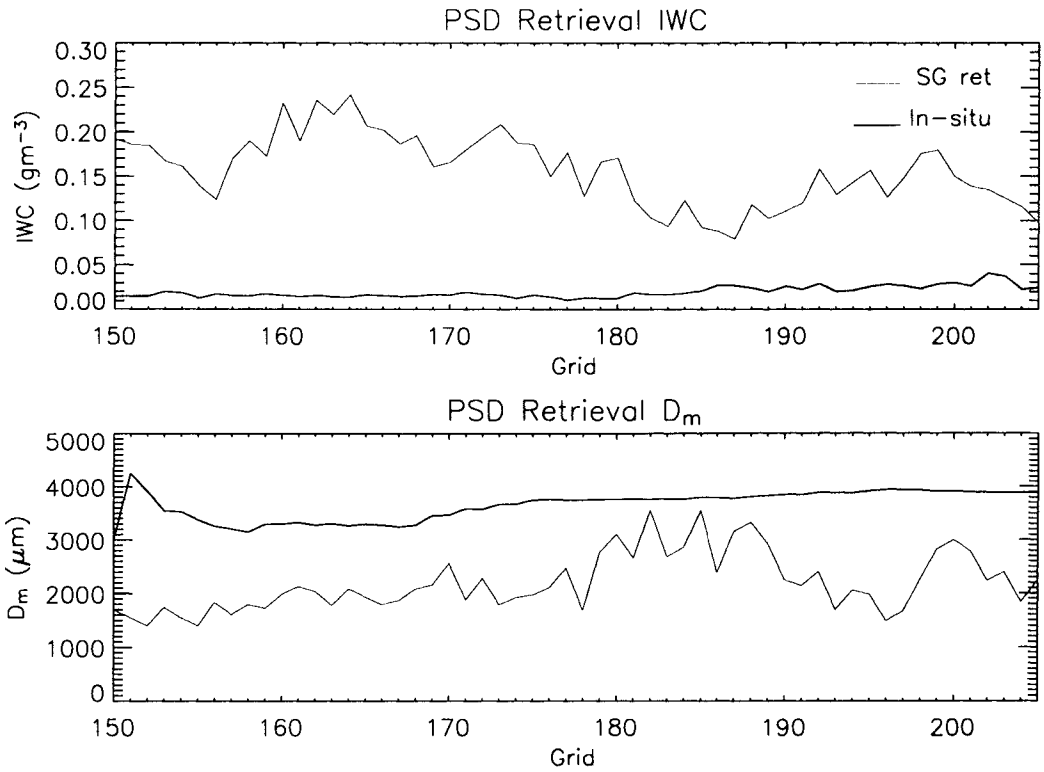

Figure 6.2 The retrieved ice water content and mean volume diameters compared to the *in situ* for each gridpoint across the cloud using the default assumptions of spherical particles and a Brown and Francis size-density.

The radar reflectivity observations are related to the retrieved PSD through the forward radiative transfer model. The differences between the radar retrieved PSD and the *in situ* measured PSD may point to uncertainties in the forward model. The first step to examine the relationship between the retrieved PSD and the *in situ* observations was operating directly on the *in situ* measurements with the forward model and comparing **F(x)** (forward modeled *in situ*) to **y** (radar observations). Using the default model assumptions of spherical particles and a Brown and Francis size-density relationship, the forward model operated on the *in situ* data to produce the **F(x)** at a grid point. Utilizing

this procedure on successive grid points in the scene produced a flight line of **F(x)** that can be compared to the remote sensing observations **y**.

There is a significant difference between the radar observations and the **F**(*in situ*) shown in Figure 6.3 consistent with the differences shown in IWC and D_m in Figure 6.2. There are several sources of uncertainty that may have contributed to this difference.

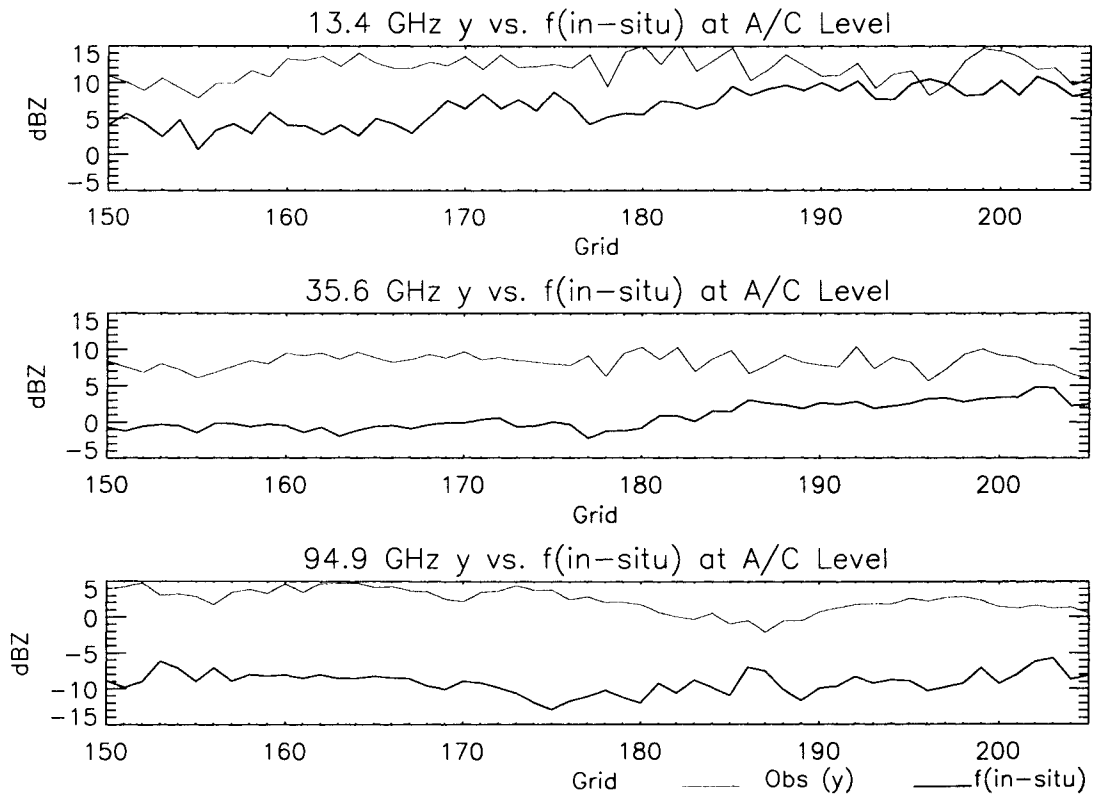

Figure 6.3. Radar observations (y) compared to forward modeled *in situ* using the default forward model assumptions of spherical particles and a Brown and Francis size-density.

There is some uncertainty due to the discontinuity in number concentrations between the two cloud probes and how they were combined to yield the *in situ* PSD. A sensitivity analysis can be performed to determine the sensitivity of the forward model to uncertainty in the *in situ* PSD. The *in situ* observations and the remote sensing

observations are not synchronous in time; there was a time lag between the observations. However, the five-minute lag between observations is not significant in the stratiform cloud under study. In addition, comparing spatially averaged observations instead of instantaneous single-grid values can minimize the effect of noise from the time lag between the observations. Finally, the assumptions in the forward model included two primary sources of uncertainty in the shape and density of the cloud ice particles. These last uncertainties can be minimized by retrieving those parameters and thus treating their associated uncertainties explicitly.

Sensitivity testing was performed to explore the effects of the PSD integration between the 2DC and 2DP instruments. The forward modeled results of a representative state (Mie spheres, Brown and Francis ice density) are shown in Table 6.1 for various PSD combinations. PSD A used the accepted methodology of a step from 2DC to 2DP at 1000 μm, PSD B used a linear interpolation over the four size bins from 800-1750 μm, and PSD C used a linear interpolation over the four size bins from 1000-2000 μm. The

Table 6.1. Radar reflectivities in dBZ for a single-grid box using various 2DC - 2DP interpolations compared to the gridded observations.

Frequency	OBS	2DC	2DP	PSD A	PSD B	PSD C
13.4 GHz	13.4	12.3	14.0	14.0	14.1	14.3
35.6 GHz	8.9	10.7	3.4	3.9	5.1	6.1
94.9 GHz	1.3	-1.3	-11.4	-6.0	-3.3	-2.4

uncertainty in PSD, especially on an individual grid point level, due to the integration of the two instruments and the resulting uncertainty in the **F(*in situ*)** reflectivities is evident. At 94.9 GHz, the reflectivity varies from –11.4 to –1.3 dBZ by selecting various combinations of the PSD. The APR-2 frequencies showed lesser but still significant

variance. The testing of distinct combinations of 2DP and 2DC PSDs could not produce a satisfactory match of the **F**(*in situ*) to the radar observations.

One method to address the uncertainty from assumptions in the forward model is to retrieve their values. Therefore, an optimal estimation framework was established to 'fit' the forward model to both the remote sensing observations (**y**) and the *in situ* observations (here a given state), using the density-size relationship and aspect ratio of oblate ice spheroids to investigate the differences between *in situ* and remote sensing observations. The first retrieval parameter was the exponential factor in the ice particle density-size relationship:

$$\rho(D) = 0.07 * D^{-\alpha} \tag{6.1}$$

where D is the semi-major axis of an oblate spheroid. Thus the density relationship returns the density of an ice particle with radius $D/2$ up to a maximum density equal to the density of pristine ice at 0.917 kg m^{-3}. The second retrieval parameter is the aspect ratio of an oblate spheroid in the T-matrix scattering code indicating the particle's departure from sphericity.

Two retrieval approaches were available to examine the differences identified between the remote sensing observations and the forward modeled *in situ*. The first approach was to fit the observations at all-grid points simultaneously to find a single overall optimal density and nonsphericity for the entire cloud. The second fits each individual grid point with its own optimal density and aspect ratio.

The all-grid optimal estimation retrieves an optimal density parameter and aspect ratio and respective uncertainties as shown in Table 6.2. The overall χ^2 of 109 for the all-grid optimal parameters is much larger than the number of degrees of freedom ($d_s = 2$)

indicating that the instantaneous fit at each grid point is not particularly good. Due to the non-synchronicity of the observations, however, a perfect instantaneous match is not expected.

Table 6.2. Shows the retrieved parameters for a variety of difference retrieval methods, the χ^2 fit of the retrieval and the RMS error **y** - **F(x)**.

Retrieval	α	a/b	χ^2	RMS		
				13.4	35.6	94.9
B&F spheres	1.1	1.0	1451	6.0	7.8	11.7
All-Grid (AG)	1.58	0.53	109	2.9	2.1	2.1
Single-Grid Mean (SGM)	1.42	0.58	132	3.0	2.2	2.7

The error covariance, $\mathbf{S_y}$, was allowed to vary in order to explore what observation error covariance was required to produce the best fit as evaluated by the χ^2 test for the retrieval. $\mathbf{S_y}$ = 15 dBZ was required to achieve $\chi^2 \sim d_s$, as shown in Table 6.3. This is significantly larger than the uncertainty in the radar reflectivities.

Table 6.3. Shows the variation in all-grid retrieved parameters and overall χ^2 as a result of relaxing the input $\mathbf{S_y}$ covariance.

$\mathbf{S_y}$	x_1	x_2	χ^2
2 dBZ	1.58	0.53	247
3 dBZ	1.58	0.53	109
5 dBZ	1.58	0.53	42
10 dBZ	1.56	0.54	12
15 dBZ	1.52	0.55	2

However, the mean reflectivities for the flight line indicated a better fit in the mean sense, as shown in Table 6.4. The all-grid retrieval provided for a representative density and shape for the cloud as a whole. But, the all-grid retrieval cannot capture any

trends or changes in the underlying microphysical characteristics within the cloud. Note also that the all-grid retrieval is over constrained, i.e., there are more observations than there are free variables and the result is evident in the high χ^2 value for the retrieval. The variability in the instantaneous values of the all-grid **F(x)** in Figure 6.4 was the result of variability in the *in situ* data and not of any attempt to match each individual grid point.

Table 6.4 Shows the cloud mean (average of all ice cloud grid points) observations and retrieval f(x) at each radar frequency for a variety of retrieval methods. 1: Brown and Francis spheres, 2: All-grid retrieval, 3: Single-grid mean retrieval, 4: Single-grid retrieval (allowing independent retrieval parameters at each grid point).

Frequency	Mean Obs	Mean				RMS			
		1	2	3	4	1	2	3	4
13.4 GHz	11.9	6.6	11.6	11.9	12.0	6.0	2.9	3.0	0.5
35.6 GHz	8.3	0.8	8.4	7.9	8.0	7.8	2.1	2.2	0.7
94.9 GHz	2.3	-9.1	2.4	0.6	0.9	11.7	2.1	2.7	1.4

The second approach utilized a retrieval at each grid point individually, thus attempting to fit the forward modeled **F(x)** to the remote sensing **y** at each point and producing an individual density and aspect ratio for every grid point. This approach allowed examination of state parameter differences through the length of the cloud and may capture intra-cloud changes in the underlying microphysics.

The individual grid retrievals enabled remarkable matching of the retrieved reflectivities to the observed reflectivities as seen in Figure 6.4. This was in direct contrast to the all-grid retrieval where the variability in **F(x)** was driven by variability in the *in situ* data. The forward modeled reflectivities now matched the maxima, minima, and overall trend of the remote sensing observations. As a result, the root mean square

(RMS) error between **F(x)** and **y** was reduced in comparison to the all-grid retrieval. However, examination of the variability of the retrieved parameters across the flight line indicated the retrieval was using the retrieved density as a 'tuning knob' to fit the curves as evidenced by the unphysical variation in the density parameter across the cloud (Figure 6.5). The maximum and minimum retrieved single-grid densities are shown in Figure 6.6 and compared to the default Brown and Francis density and the all-grid retrieved density.

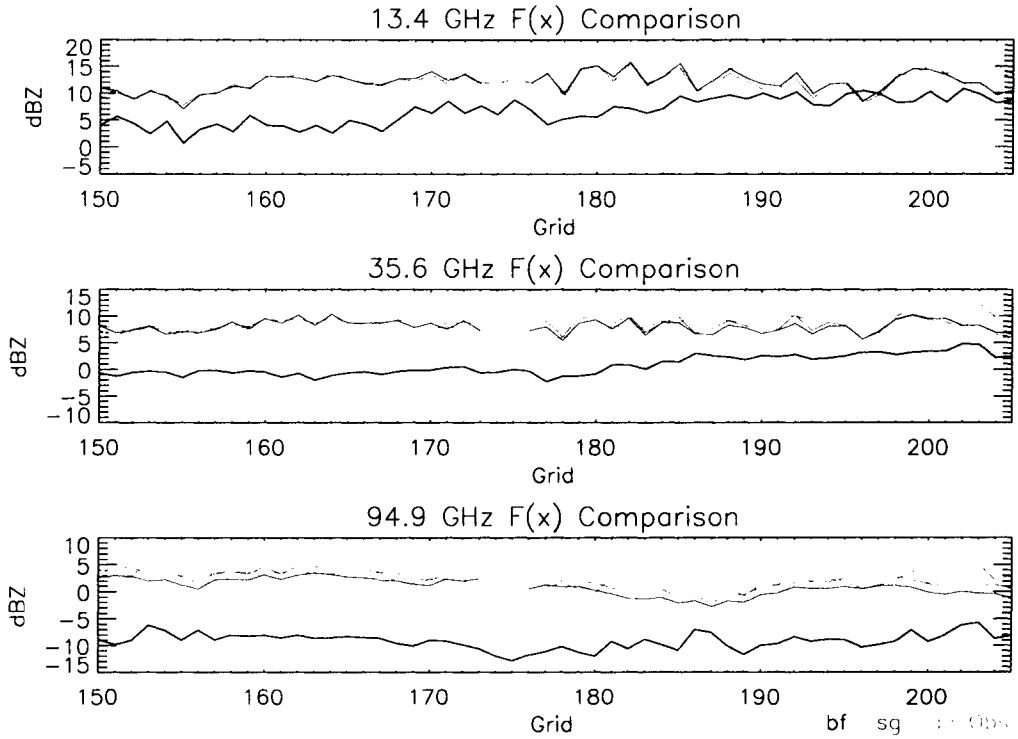

Figure 6.4. Radar observations compared to forward modeled *in situ* using different model assumptions. Obs represents the observed reflectivities. AG represents a single all-grid optimal value of density parameter and aspect ratio. SG represents the single-grid optimal values of density and aspect ratio for each grid point. BF represents the default values of Brown and Francis density and spherical particles.

Finally, although the 13.4 and 35.6 GHz **F(x)** matched the observations quite well, there was a negative bias in the 94.9 GHz single-grid **F(x)** indicating that perhaps

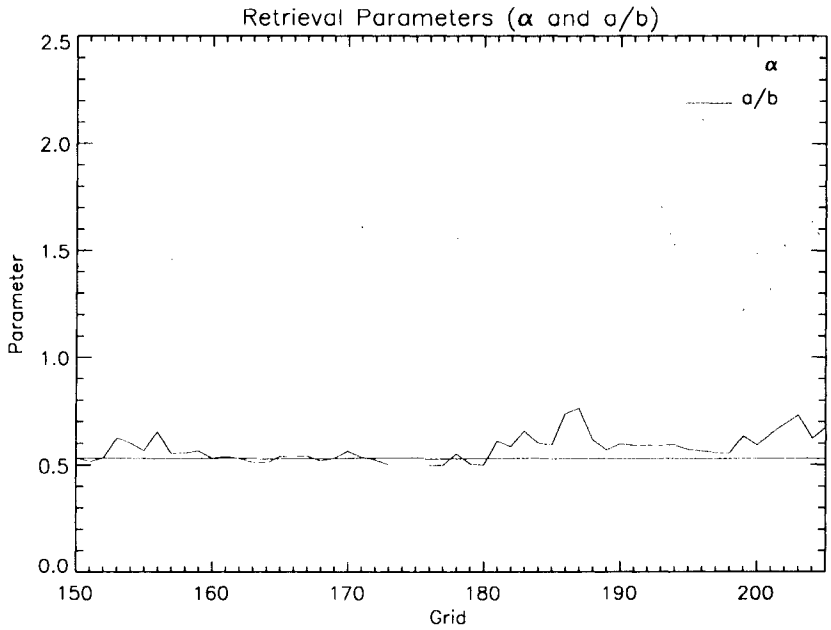

Figure 6.5. Plot of the optimally retrieved parameters for the single-grid retrieval compared to the values of the all-grid retrieval. The constant lines across the plot are the all-grid retrieved values while the lines that are variable across the plot are the single-grid retrieved values.

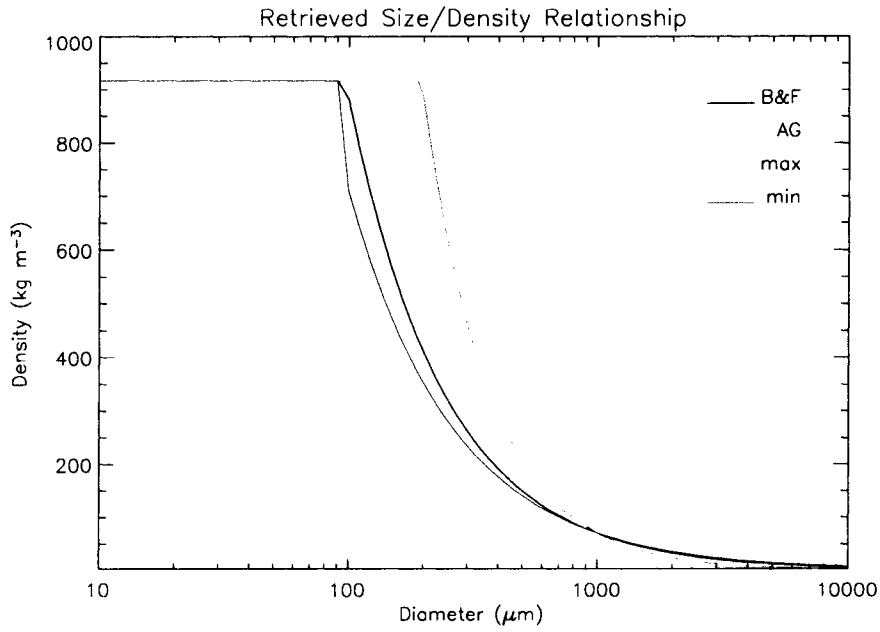

Figure 6.6. Retrieved size density relationships compared to the default Brown and Francis size density relationship. B&F is Brown and Francis, AG ret is the all-grid optimally retrieved density, SG max and SG min represent the maximum and minimum retrieved densities for the single-grid optimal retrieval.

the *in situ* measurements were not quite correct either in undercounting the small particles or in the combination of the 2DC and 2DP data to create the overall PSD.

Exploring the sensitivity of the forward model to changes in the assumptions of density and nonsphericity proved that these two parameters can account for the original differences between the remote sensing observations and the forward modeled *in situ*. Therefore, the PSD retrieval was repeated using the retrieved optimal density and aspect ratio as improved assumptions in the forward model. Figure 6.7 shows the results of this PSD retrieval. While no longer fully independent, the retrieved normalized gamma PSD matches the *in situ* PSD quite well. The main deviation of the gamma PSD from the *in situ* occurs at the smallest particles, where the retrieved PSD indicates a greater concentration of small particles than is seen by the *in situ* 2D probes.

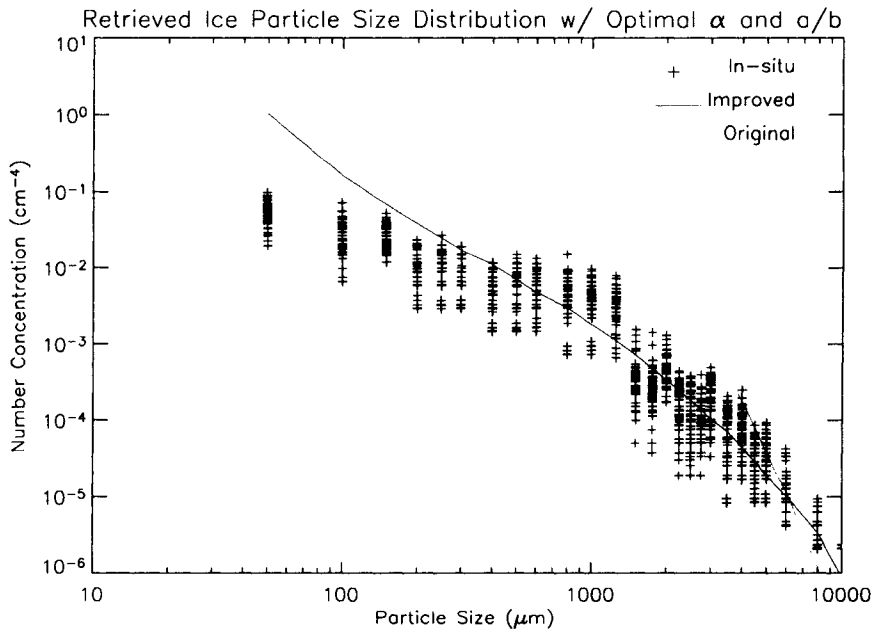

Figure 6.7. Improved assumption PSD retrieval compared to the *in situ* observed PSD. The improved assumption retrieval incorporated the all-grid optimal values for the density-size relationship and particle aspect ratio.

CHAPTER 7

VERTICAL PROFILE PSD RETRIEVAL

From the discussion of the radiative transfer model, the retrieval state for the clear sky case considered the sea surface (or skin) temperature, surface wind speed, temperature lapse rate, and a column value for relative humidity. In addition, the freezing level was identified from the bright band in the radar data for the flight line and was fixed at 1950 m. For the cloudy scene, the state vector adds the three components of the normalized gamma PSD at every cloudy level. The base and top of the clouds are determined by the presence of a valid 94.9-GHz echo in the lowest and highest vertical levels. If there is no valid echo at 13.4 or 35.6 GHz at any level, the respective **y** value for that level is set equal to the ACR reflectivity and is unweighted in the retrieval scheme by setting its $\mathbf{S_y}$ to 1000^2.

The mechanics of the optimal estimation retrieval rely first on the specification of the *a priori* $\mathbf{x_a}$, and the input error covariances $\mathbf{S_a}$ and $\mathbf{S_y}$. The values for $\mathbf{x_a}$ were determined from the climatology of the Wakasa Bay area and from concurrent satellite observations. For the clear sky case, $\mathbf{x_a}$ = [285 K, 10 m s^{-1}, 6 K km^{-1}, 50% RH]. Assignment of $\mathbf{S_a}$ in combination with $\mathbf{x_a}$ just discussed produces the PDF describing the knowledge of possible states for each parameter in the state vector where $\mathbf{x_a}$ is the mean

of the distribution and the diagonal elements of $\mathbf{S_a}$ represent the width or variance (σ^2) of the distribution. For the clear sky case, the diagonal elements of $\mathbf{S_a}$ = [10^2 K, 10^2 m s^{-1}, 5^2 K km^{-1}, 40^2 % RH]. For example, the PDF of possible sea surface temperatures is described by the Gaussian distribution represented by a mean of 285 K and a standard deviation of 10 K. $\mathbf{S_y}$ represents the uncertainty around the measurement **y** in a similar manner when the measurement is described by a PDF of possible states where **y** is the mean value and $\mathbf{S_y}$ is the width of the measurement PDF. For the clear sky case (MIR only) $\mathbf{S_y}$ is [3^2, 3^2, 3^2, 3^2, 3^2, 5^2, 7^2] where the $\mathbf{S_y}$ around the highest MIR frequencies accounts for the greater instrument noise in those channels. For example, if the measured 89-GHz brightness temperature for a grid point is 220 K, then the measurement PDF is described by a Gaussian distribution with mean 220 K and standard deviation 3 K. For the cloudy case, $\mathbf{x_a}$ and $\mathbf{S_a}$ must include values for the normalized gamma PSD parameters, μ, N_o^*, and D_m. For the PSD parameters, $\mathbf{x_a}$ = [-1.0, 1.0 x 10^6, 1.0 x 10^{-3}] from a general fit of a normalized gamma function to the distribution of *in situ* PSDs found in the ice cloud as described in chapter six. To complete the PDF of possible states, $\mathbf{S_a}$ must be defined for the PSD parameters. As for the background emission parameters defined previously in the clear sky discussion, the diagonal of $\mathbf{S_a}$ is defined by a range of possible parameters that provide gamma curves falling within the *in situ* PSDs. $\mathbf{S_a}$ for the PSD parameters is defined as [1^2, $(1.0 \times 10^8)^2$, $(1.0 \times 10^{-3})^2$]. But, in contrast to the background emission parameters, $\mathbf{S_a}$ for the PSD is not defined as a diagonal matrix. A correlation scale length between layers is defined to introduce a requirement that the PSD vary smoothly between layers. From Rodgers (2000) a correlation constraint can be defined as:

$$\mathbf{S}_{ij} = \sigma_a^{\,2} \exp(-|i-j|\frac{\delta z}{h}) \qquad (7.1)$$

Where δz is the vertical level spacing and h is the scale length for the parameter. For the ice cloud under study δz = 150 m and h was defined at 500 m.

The retrieval was first performed for the clear sky scene. The clear sky scene is the simplest case for retrieval and provides a validation of the retrieval methodology and the modeling of the background emission. The first attempt at clear sky retrieval failed to converge to a solution. For the clear sky case there are no radar observations so the retrieval uses only the MIR and PSR radiometer observations. The retrieval was next performed using only the observations from the MIR sensor, and this time it successfully converged to a solution state. The retrieval was then attempted using only the observations from the PSR sensor and again failed to converge. The MIR and PSR share the 89-GHz frequency and so the two instruments were compared to determine the obstacle to retrieval convergence. The 89-GHz observations from both the MIR and PSR are compared in Figure 7.1. There is a discrepancy between the PSR and the MIR instrument, which share the 89-GHz frequency. The two instruments show the same general features, e.g., one can visually match the traces by the features in the flight line. However, the PSR shows a consistent cold bias relative to the MIR observations of up to 10 K in many places through the flight line.

An experiment was then performed to determine if the bias was only in the PSR 89 GHz or the other PSR channels as well. The MIR retrieved state was assumed as the true state. Then the forward model operated on the assumed true state to produce synthetic observations at the PSR frequencies, which would be consistent with the MIR observations. The results for a sample individual grid point are shown in Table 7.1.

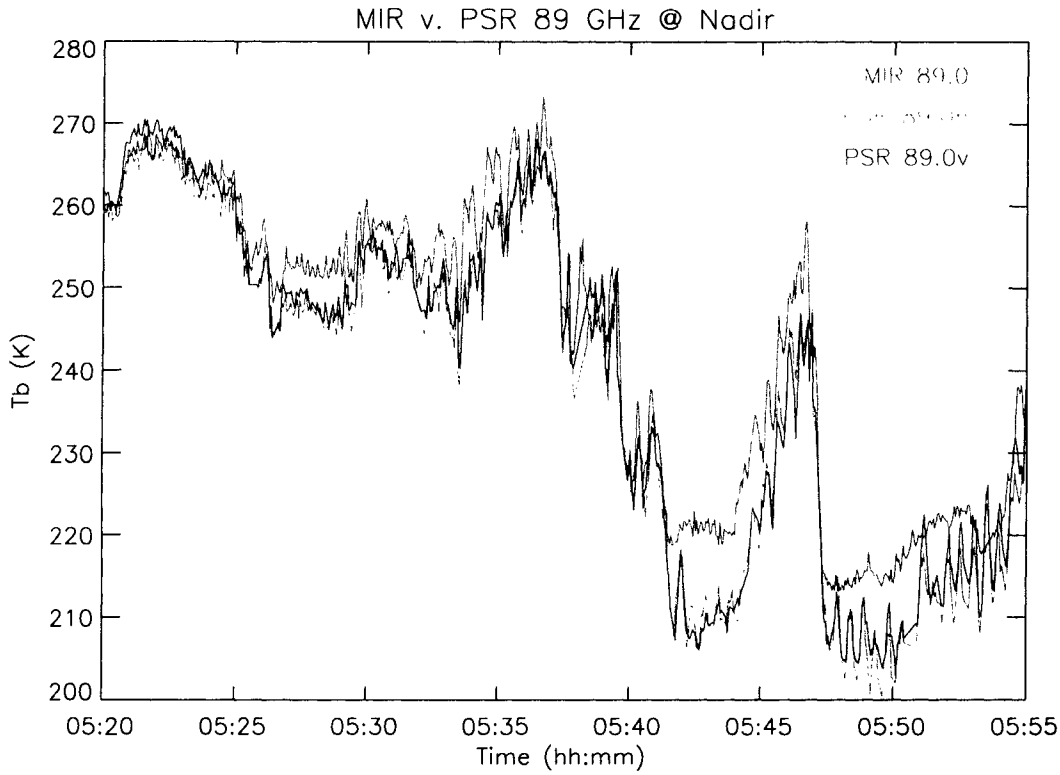

Figure 7.1. MIR v. PSR 89 GHz raw brightness temperatures across the entire flight line.

Table 7.1 Bias between PSR observations and synthetic PSR TBs consistent with MIR observations.

Instrument	10.7 GHz	18.7 GHz	21.5 GHz	37 GHz	89 GHz
PSR	130.5 K	143.9 K	167.5 K	171.5 K	209.7 K
$F(x_{MIR})$	118.0 K	135.3 K	154.5 K	161.3 K	214.4 K
Bias	+12.5 K	+8.6 K	+13.0 K	+10.2 K	-4.7 K

Although the PSR 89 GHz showed a cold bias relative to the MIR, the other frequencies of the PSR showed a warm bias relative to the synthetic PSR observations. This internally inconsistent bias across the PSR frequencies could be the source of the PSR-only retrieval's failure to converge. In order to test this possibility, the 89-GHz observations were removed as inputs to the PSR-only retrieval. This time the retrieval successfully converged to a solution, however the retrieved state was unreasonably warm,

consistent with the bias in the first four PSR frequencies. The PSR retrieved state is attempting to find warmer conditions than exist by increasing T_{sfc}, V_{sfc}, RH and decreasing lapse rate. Table 7.2 shows the MIR retrieved state and the PSR (without 89 GHz) retrieved state.

Table 7.2. Comparison between MIR-only retrieved state and PSR-only (without 89 GHz) retrieved state.

Retrieval state	T_{sfc} (K)	V_{sfc} (m s^{-1})	LR (K km^{-1})	RH (%)
MIR	286.5	8.6	5.2	69.9
PSR	289.6	16.9	3.6	75.1

The physical consistency enforced through the optimal estimation methodology identified instrument calibration issues that otherwise may have gone unnoticed. When presented with a set of inconsistent observations the retrieval failed to converge. The PSR calibration issues were identified to the PSR team and addressing this calibration is an area of ongoing research. The decision was then made to exclude the PSR observations from the retrieval and use only the MIR observations as the passive microwave input.

The MIR-only clear sky retrieval is shown in Table 7.3 along with the optimal estimation and information content diagnostics. The retrieval values seem reasonable when compared to the climatology and concurrent observations of the region. The retrieved uncertainty is given by the standard deviation of the retrieved values. Recall that the optimal estimation retrieval produces not a single retrieved value but a PDF of retrieved possible states with the mean of the PDF as the retrieved value and the width of the distribution as the uncertainty. The A-matrix output from the optimal estimation method describes the contribution towards the retrieved state from the *a priori* and the observations. An A-matrix value of zero indicates that the retrieval relied solely on the *a*

priori to determine that retrieval parameter and an A-matrix value of one indicates the retrieval parameter was determined completely by the observations. H_x is the information content for each retrieved parameter.

Table 7.3. Clear sky retrieved state with optimal estimation and information content diagnostics: σ is the standard deviation of the retrieved parameters, A is the A-matrix values from 0 to 1, H_x is the individual parameter Shannon Information Content.

	T_{sfc} (K)	V_{sfc} (m s^{-1})	LR (K km^{-1})	RH (%)
Retrieved	286.5	8.6	5.2	69.9
σ	7.7	5.6	1.2	16
A	0.41	0.68	0.94	0.85
H_x	0.39	0.83	2.1	1.4

Once the retrieval methodology had been validated during the clear sky retrieval, the ice cloud could be considered. The extent of the cloud was entirely above the freezing level and thus showed no sign of the bright band evident in other areas of the flight line. The pilot of the P-3 aircraft gathering the data reported no icing during this flight indicating the absence of supercooled water. Therefore, the retrieval assumed there was no supercooled water in the cloud and retrieved a PSD for cloud ice particles only.

Using the default model assumptions of ice spheres and a Brown and Francis size-density relationship, the retrieval was applied to the ice cloud scene. Retrieving for each grid point through the extent of the cloud from grid points 150 to 205 produced the background emission state parameters plus a vertical profile of PSDs for each grid point. Figure 7.2 shows the composite of vertical profiles of retrieved PSD parameters along with the cloud mean vertical profile for each parameter. Also shown in Figure 7.2 are the composite and cloud mean vertical profiles of retrieved ice water content. A

representative grid point retrieval for grid point 201 is shown in Table 7.4 for the emission parameters and the retrieved PSD parameters are shown in Tables 7.5.

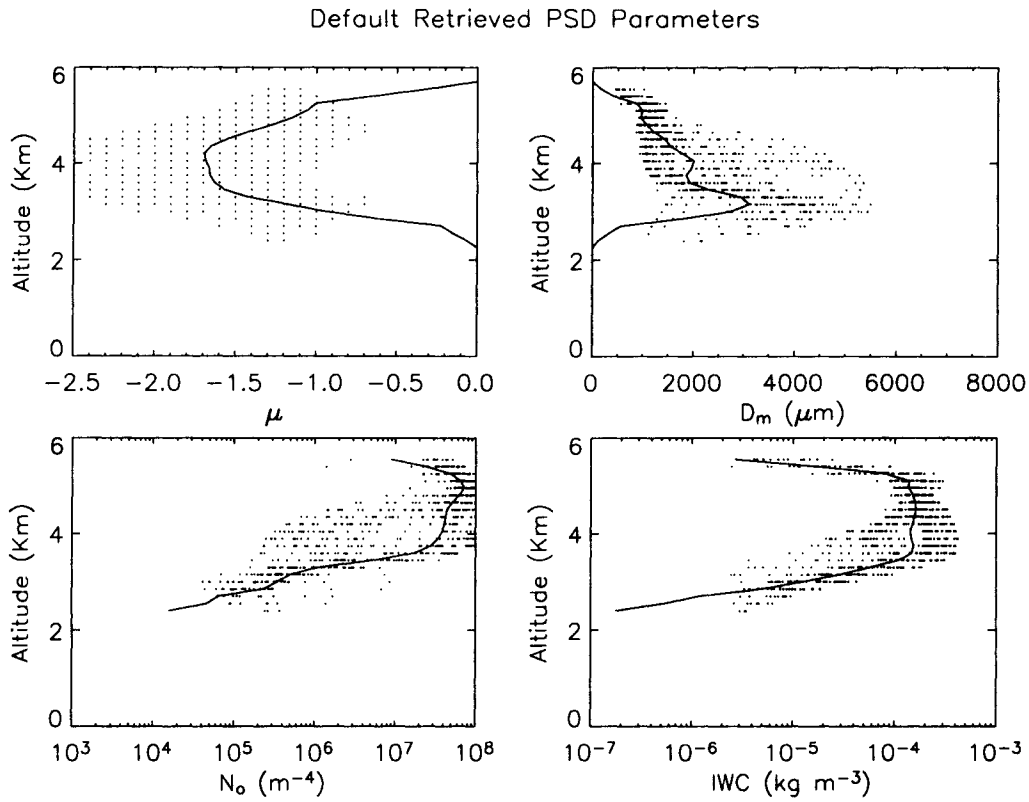

Figure 7.2. Default model (Brown and Francis ice size-density relationship and spherical particles) retrieved normalized gamma PSD profiles for the ice cloud from grid point 150 to 205.

Table 7.4. Default model retrieved emission parameters with uncertainties and A-matrix diagnostics.

	T_{sfc} (K)	V_{sfc} (m s^{-1})	LR (K km^{-1})	RH (%)
Mean	284.2	11.6	7.1	68
σ	7.8	5.9	1.3	23
A	0.39	0.66	0.93	0.67

Table 7.5. Default model retrieved PSD parameters, uncertainties and optimal estimation diagnostics.

Layer	μ	N_o^*	D_m	$\sigma\mu$	σN_o^*	σD_m	A μ	A N_o^*	A D_m
Top	-1.1	4.25E7	4.93E-4	.99	9.6E7	2.6E-4	0.00	0.00	1.0
16	-1.2	5.83E7	8.26E-4	.99	9.2E7	3.7E-4	0.00	0.02	0.98
15	-1.2	7.84E7	1.15E-3	.98	8.6E7	4.2E-4	0.01	0.05	0.96
14	-1.3	1.00E8	9.72E-4	.97	7.8E7	1.8E-4	0.02	0.17	1.0
13	-1.4	9.25E7	1.08E-3	.95	7.0E7	2.0E-4	0.02	0.20	0.99
12	-1.6	7.56E7	1.17E-3	.94	6.2E7	2.3E-4	0.02	0.25	0.99
11	-1.8	4.60E7	1.33E-3	.92	4.7E7	3.3E-4	0.03	0.44	0.97
10	-2.0	6.58E6	2.32E-3	.88	8.4E6	7.9E-4	0.08	0.98	0.80
9	-2.0	2.17E6	2.98E-3	.85	2.8E6	1.1E-3	0.13	1.0	0.68
8	-2.0	9.86E5	3.43E-3	.83	1.3E6	1.2E-3	0.17	1.0	0.60
7	-1.8	4.85E5	3.70E-3	.84	5.8E5	1.3E-3	0.19	1.0	0.57
6	-1.6	5.81E6	3.10E-3	.91	7.0E5	1.0E-3	0.03	1.0	0.72
5	-1.4	1.10E6	2.44E-3	.95	1.3E6	7.4E-4	0.00	1.0	0.83
4	-1.3	2.33E6	1.93E-3	.98	2.7E6	5.8E-4	0.00	1.0	0.89
3	-1.2	2.67E6	1.85E-3	.99	3.2E6	5.6E-4	0.00	1.0	0.93
2	-1.2	1.60E6	1.63E-3	.99	5.7E6	2.1E-3	0.00	0.99	0.01
Base	-1.1	7.32E5	1.46E-3	1.0	3.7E6	2.5E-3	0.00	1.0	0.00

The χ^2 for the default model retrieval for grid point 201 was 13.6. χ^2 evaluates the 'goodness' of fit when compared to the number of independent parameters in the retrieval. If χ^2 is much greater than n, then the input covariance may be underestimated and the retrieved covariance would also be underestimated. If χ^2 is much less than n, then the input covariances may be overestimated and the retrieved covariance would also be overestimated.

The number of independent parameters (n) required for comparison with χ^2 can be estimated in different ways. The total number of retrieved parameters is three PSD parameters per cloud layer plus the four background parameters, which in this 17-layer grid point equals 55. However, the effective rank was calculated through an information content analysis to be $N = 28$. This indicates that not every retrieved parameter is

independent and χ^2 would be better compared against $n = 28$. In this case, $\chi^2 = 13.6$ is on the same order as $n = 28$, thus indicating a relatively good fit.

An information content analysis was performed on the default model retrieved grid point. The results of the information content analysis were: effective rank (N) = 28, degrees of freedom for signal (d_s) = 27.4, and the Shannon Information Content (H) = 123.6. As discussed in the previous paragraph, the effective rank represents the number of independent retrieved parameters, where N less than the total number of retrieved parameters indicates that not every retrieved parameter is independent. Similarly, the degrees of freedom for signal (d_s) = 27.4 represents the number of independent measurements. This can be compared to the total number of measurements, $27.4 < 58$, indicating that not all of the measurements are independent. The Shannon Information Content represents the reduction in uncertainty from the *a priori* state to the retrieved state as a result of the measurement. $H = 123.6$ means that $2^{123.6}$ (1.6×10^{37}) total possible states can be determined by the measurements out of the *a priori* state space.

In addition, the information content for each individual parameter was computed. The H_x, or information about each parameter is H_x = [0.361, 0.772, 1.95, 0.798] for the T_{sfc}, V_{sfc}, LR, and RH parameters. Not much information about the surface emission parameters is available from the measurements. This result is expected with the loss of the lower frequency PSR data; the higher frequencies of the MIR instrument are not as sensitive to changes in the surface emission. The lapse rate parameter shows the most information content as would be expected for its impact on the distribution of upper level moisture, to which the MIR observations are sensitive. The H_x for the PSD components contributes most to the total information content as shown in Table 7.6.

Table 7.6. Shannon Information Content (H) and individual parameter information content (H_x) for the default model retrieval.

Level	H_x (μ)	H_x (N_o^*)	H_x (D_m)	H
Top	0.00947	0.0621	3.53	3.60
16	0.0173	0.116	3.03	3.16
15	0.0309	0.209	2.83	3.07
14	0.0500	0.366	4.06	4.47
13	0.0689	0.506	3.91	4.48
12	0.0915	0.688	3.69	4.46
11	0.126	1.08	3.17	4.38
10	0.185	3.57	1.93	5.69
9	0.242	5.16	1.49	6.89
8	0.270	6.32	1.27	7.86
7	0.246	7.44	1.24	8.93
6	0.133	7.16	1.57	8.87
5	0.0686	6.31	2.02	8.40
4	0.0361	5.20	2.37	7.61
3	0.0197	4.98	2.42	7.42
2	0.0108	4.12	0.549	4.68
Base	0.00588	4.75	0.250	5.01

Next the ice cloud retrieval was performed for the same subset of grid points using the optimal assumption model. The optimal model used the optimally derived size-density relationship and oblate spheroid aspect ratio derived in chapter six as improved assumptions in the forward radiative transfer model. Figure 7.3 shows the composite of retrieved profiles plus the cloud mean profile for each parameter. In addition the composite and cloud mean ice water content profiles are shown.

The optimal retrieval at a representative grid point shown in Table 7.7 may be compared to the previous default retrieval at the same grid point in Table 7.4. The retrieved emission state parameters are almost identical. However, the optimal retrieval of vertical PSD profiles is significantly different than the default retrieval shown in Table 7.5. Table 7.8 shows the optimal retrieval of PSD parameters for grid point 201.

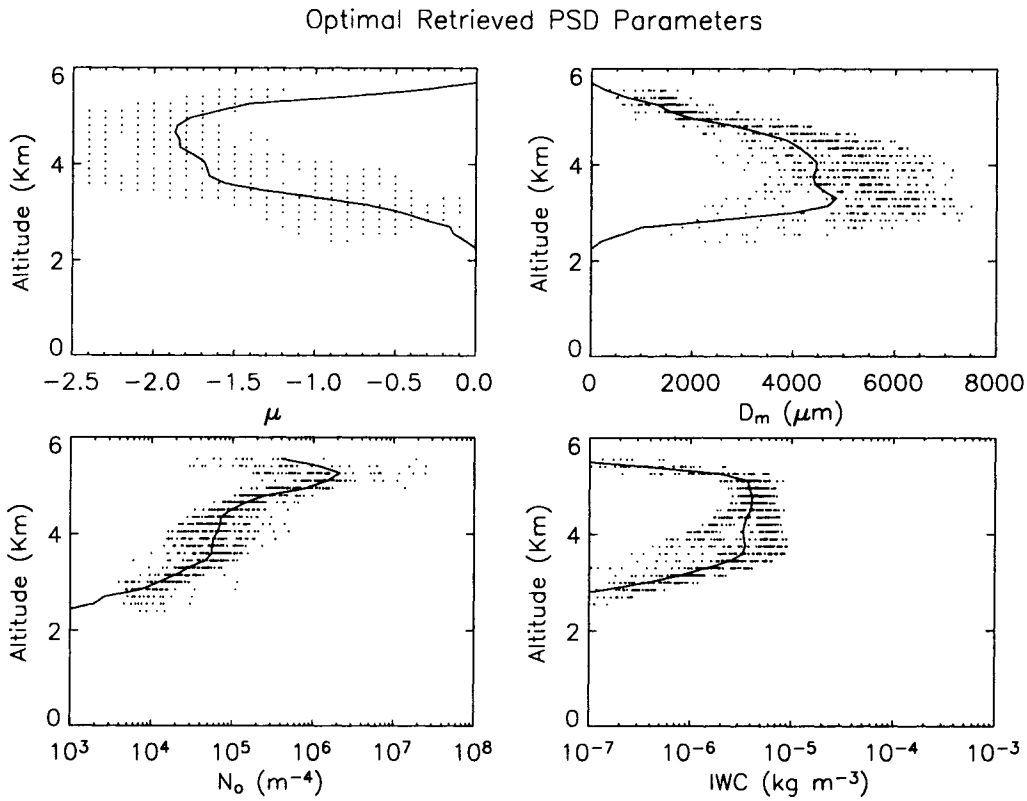

Figure 7.3. Optimal model (optimal ice size-density and oblate spheroid aspect ratio from Part One) retrieval of normalized gamma PSD profiles for the ice cloud from grid point 150 to 205.

Table 7.7. Optimal model retrieved emission parameters with uncertainties and A-matrix diagnostics.

	T_{sfc} (K)	V_{sfc} (m s^{-1})	LR (K km^{-1})	RH (%)
Mean	284.6	11.9	7.1	67.2
σ	7.8	5.8	1.3	23
A	0.39	0.67	0.93	0.66

Table 7.8. Optimal model retrieved PSD parameters, uncertainties and optimal estimation diagnostics.

Layer	μ	N_o^*	D_m	$\sigma\,\mu$	$\sigma\,N_o^*$	$\sigma\,D_m$	A μ	A N_o^*	A D_m
Top	-1.5	5.68E4	1.38E-3	.96	3.2E5	2.7E-3	0.00	1.0	0.00
16	-1.7	4.50E5	1.51E-3	.93	2.1E6	2.5E-3	0.00	1.0	0.00
15	-1.9	1.46E6	1.70E-3	.88	5.1E6	2.0E-3	0.03	0.99	0.02
14	-2.3	7.91E5	2.03E-3	.79	9.7E5	6.4E-4	0.15	1.0	0.93
13	-2.4	2.86E5	2.94E-3	.72	4.0E5	1.1E-3	0.24	1.0	0.64
12	-2.4	2.86E5	2.94E-3	.69	3.0E5	1.4E-3	0.26	1.0	0.55
11	-2.2	1.21E5	3.95E-3	.67	1.7E5	1.6E-3	0.29	1.0	0.46
10	-1.8	7.46E4	5.08E-3	.64	9.1E4	1.9E-3	0.38	1.0	0.31
9	-1.5	4.99E4	5.60E-3	.64	5.6E4	2.0E-3	0.38	1.0	0.30
8	-1.3	3.64E4	5.80E-3	.65	3.9E4	2.0E-3	0.38	1.0	0.31
7	-1.0	2.54E4	5.74E-3	.70	2.6E4	1.9E-3	0.36	1.0	0.35
6	-0.9	2.43E4	4.99E-3	.80	2.7E4	1.7E-3	0.20	1.0	0.46
5	-0.9	3.30E4	4.15E-3	.88	3.8E4	1.4E-3	0.10	1.0	0.62
4	-0.9	4.93E4	3.46E-3	.93	5.5E4	1.1E-3	0.04	1.0	0.76
3	-0.9	5.78E4	3.28E-3	.96	6.4E4	1.0E-3	0.04	1.0	0.83
2	-0.9	3.41E4	2.69E-3	.98	5.9E4	2.1E-3	0.00	1.0	0.00
Base	-0.9	1.64E4	2.25E-3	.99	4.1E4	2.6E-3	0.00	1.0	0.00

The χ^2 for the optimal retrieval was 14.3, very close to the χ^2 of the default retrieval at this grid point. An information content analysis was performed for the optimal retrieval. The results of the information content analysis were: effective rank (N) = 29, degrees of freedom for signal (d_s) = 29.0, and the Shannon Information Content (H) = 210.9. While the degrees of freedom showed a slight increase, the information content increased dramatically indicating significantly reduced uncertainty in the retrieval state. The increase in H means that $2^{87.3}$ (1.9×10^{26}) more states can be resolved by the optimal retrieval than the default retrieval. In addition the information content for each individual parameter was computed. The H_x, or information about each parameter is H_x = [0.359, 0.797, 1.94, 0.778] for the T_{sfc}, V_{sfc}, LR, and RH parameters. These results were quite similar to the default retrieval, indicating again that most of the information in the

observations is going toward the PSD component retrieval. The H_x for the PSD components is shown in Table 7.9.

Table 7.9. Shannon Information Content (H) and individual parameter information content (H_x) for the optimal model retrieval.

Level	H_x (μ)	H_x (N_o^*)	H_x (D_m)	H
Top	0.0537	8.27	0.130	8.45
16	0.101	5.54	0.256	5.90
15	0.189	4.30	0.554	5.04
14	0.343	6.69	2.24	9.27
13	0.472	7.98	1.41	9.85
12	0.531	8.37	1.10	10.0
11	0.581	9.18	0.869	10.6
10	0.652	10.1	0.650	11.4
9	0.655	10.8	0.576	12.0
8	0.611	11.3	0.578	12.5
7	0.514	11.9	0.642	13.1
6	0.328	11.8	0.813	13.0
5	0.190	11.4	1.12	12.7
4	0.102	10.8	1.48	12.4
3	0.0654	10.6	1.58	12.3
2	0.0352	10.7	0.483	11.2
Base	0.0191	11.2	0.225	11.5

The information content can also be examined for the contributions from individual elements of **y**, such as a single frequency, or sets of **y** elements, such as the information content from the MIR instrument. Table 7.10 shows the information content for the grid point 201 retrieval from different subsets of **y**. One intuitive result is that the radar observations provide no information about the surface emission parameters T_{sfc} and V_{sfc}. This does not imply that radars have no useful information about T_{sfc} or V_{sfc}, only that the surface cross-section was not used in this study and that the reflectivity from the cloud volume provides no information about the surface. Another intuitive result is that the radar observations provide most of the information about the vertical distribution of

Table 7.10. Optimal retrieval observation subset information content for grid point 201. PSD parameters are mid-cloud.

Y subset	H	$H(T_{sfc})$	$H(V_{sfc})$	H(LR)	H(RH)	$H(\mu)$	$H(N_o^*)$	$H(D_m)$
All obs	211	0.359	0.797	1.94	0.778	0.655	10.8	0.576
MIR	23.1	0.0459	0.452	0.931	0.433	5.26E-5	1.45	4.30E-5
All radar	205	0.0	0.0	1.31E-3	4.40E-6	0.646	10.8	0.571
94.9 GHz	182	0.0	0.0	1.65E-8	5.28E-10	2.13E-7	10.5	1.88E-4
13.4 GHz	141	0.0	0.0	6.04E-10	1.83E-13	4.25E-8	10.0	2.05E-4
35.6 GHz	106	0.0	0.0	8.86E-11	5.10E-12	1.70E-7	10.5	1.10E-4

hydrometeors through the PSD retrieval. The ACR radar at 94.9 GHz provides more information about the cloud ice PSD parameters than the lower frequency radars as would be expected. The APR-2 frequencies do provide significant information about the PSD parameters; however, it appears that the information content from each instrument is somewhat redundant as the total information content for the PSD parameters is not the additive result of each radar's contribution. For example, in the center of the cloud the total H for N_o^* for all radars is 10.79, while the three individual radars have H of 10.47, 10.00, and 10.45. The same analysis of information content for the default retrieval (Table 7.11) reveals that the total all-radar H for N_o^* at the center of the cloud is 5.15, while the three individual radars have contribute H of 4.28, 3.62, and 3.96. In contrast to the N_o^* H, the H for μ and D_m appears to be synergistic. Total μ H for all three radars is 0.646 while the individual contributions are 2.13×10^{-7}, 4.25×10^{-8}, and 1.70×10^{-7}. Likewise, total D_m H for all three radars is 0.571 while the individual contributions are only 1.88×10^{-4}, 2.05×10^{-4}, and 1.10×10^{-4}.

Table 7.11. Default retrieval observation subset information content for grid point 201. PSD parameters are mid-cloud.

Y subset	H	$H(T_{sfc})$	$H(V_{sfc})$	H(LR)	H(RH)	$H(\mu)$	$H(N_o^*)$	$H(D_m)$
All obs	124	0.360	0.772	1.95	0.798	0.242	5.16	1.49
MIR	9.56	0.222	0.681	1.89	0.760	2.06E-3	0.472	0.0661
All radar	118	0.0	0.0	2.16E-3	1.21E-5	0.232	5.15	1.49
94.9 GHz	95.9	0.0	0.0	5.88E-6	4.21E-8	7.63E-5	4.28	0.236
13.4 GHz	71.1	0.0	0.0	1.68E-7	2.74E-11	1.09E-5	3.62	0.256
35.6 GHz	44.0	0.0	0.0	4.07E-8	6.91E-10	4.79E-5	3.96	0.247

A sensitivity analysis was performed to examine the robustness of the retrieval results. Using the retrieved IWP as an indicator of the overall retrieved state for a grid point, input values were perturbed for grid point 201 and the results are shown in Table 7.12. First the impact of changing the *a priori* state was explored. The retrieval was essentially unaffected by reducing the *a priori* emission state PDF by half as all changes were well within the retrieval uncertainties. The next perturbation was to reduce the PSD

Table 7.12. Sensitivity of retrieval to changes in the *a priori* state and observations. IWC is at mid-cloud level. Perturbations: a. Cut $\mathbf{S_a}$ for the emission parameters by half; b. Cut $\mathbf{S_a}$ for PSD parameters by half; c. Change $\mathbf{x_a}$ μ from -1.0 to -1.5; d. Change $\mathbf{x_a}$ N_o^* from 1.0×10^6 to 1.0×10^5; e. Change $\mathbf{x_a}$ D_m from 1.0×10^{-3} to 1.0×10^{-4}; f. Perturb 94.9 GHz +1 dBZ at every cloud level; g. Perturb 13.4 GHz +1 dBZ; h. Perturb 35.6 GHz +1 dBZ.

Change	T_{sfc}	V_{sfc}	LR	RH	IWP	IWC
Baseline	284.6	11.9	7.1	67.2	0.521E-2	0.242E-5
a.	284.7	12.6	7.0	62.9	0.523E-2	0.244E-5
b.	284.7	11.4	6.7	70.9	0.593E-2	0.361E-5
c.	284.9	12.1	7.1	66.5	0.541E-2	0.224E-5
d.	284.6	11.9	7.1	67.2	0.523E-2	0.243E-5
e.	284.6	11.9	7.1	67.2	0.515E-2	0.244E-5
f.	285.5	12.6	7.1	65.4	0.638E-2	0.278E-5
g.	284.8	11.8	7.1	67.4	0.517E-2	0.232E-5
h.	284.3	11.6	7.0	68.0	0.504E-2	0.261E-5

parameters $\mathbf{S_a}$ by half. This again made only small changes to the surface emission parameters and made a slightly larger change in the retrieved IWP. This was the largest change evidenced in the changing of the *a priori* state. Further exploration by perturbing $\mathbf{x_a}$ mean values (μ from -1.5 to -1., N_o^* from 1.0×10^6 to 1.0×10^5, and D_m from 1.0×10^{-3} to 1.0×10^{-4}) yielded only slight deviations in the retrieved parameters.

Next the observations were perturbed by incrementing the reflectivities for each radar by +1 dBZ in turn, at every level in the cloud. Increasing the ACR 94.9-GHz reflectivity at every level in the cloud produced the greatest change in the retrieval results, a 20% increase in IWP. This is still within the retrieved IWP uncertainty. Also note the increase in T_{sfc} and V_{sfc} to compensate for the increased ice scattering in the profile while remaining true to the radiometer observations. Incrementing the other radar frequencies produced less minimal disturbance in the retrieval. Overall the retrieval results are quite robust to changes in both the *a priori* and are also stable to small changes in the observations.

CHAPTER 8

DISCUSSION

8.1 Single-Level PSD Retrieval

The initial optimal single-level retrievals of cloud ice PSDs showed significant differences from the *in situ* cloud probe measured PSDs. Retrieved number concentrations of particles showed 100 times more particles than the *in situ*. The resulting IWC was up to 10 times larger than the *in situ* while the retrieved D_m was smaller then the *in situ* D_m by half. The remote sensing observations, the forward radiative transfer model or the *in situ* observations contained errors.

Exploring the differences between *in situ* and retrieved PSDs by forward modeling the *in situ* proved illuminating. The large negative bias in the **F(x)** relative to the observations, shown in Figure 6.4, indicated that one or more of the forward model assumptions were incorrect. In this case, sensitivity testing indicated that the ice particles in this particular cloud were not Brown and Francis density spheres. Allowing the assumed size-density relationship and the aspect ratio of the ice particles to vary as retrieved parameters was able to reconcile the differences between remote sensing and *in situ* observations. Retrieving an optimal density and nonsphericity for the particles not only brought the **F**(*in situ*) in line with the remote sensing observations, but also

impacted the retrieved ice water content (Figure 8.1) where the default spheres have 2-5 times the IWC of the optimally retrieved spheroids despite the negative **F(*in situ*)** bias in the reflectivity of the default spheres.

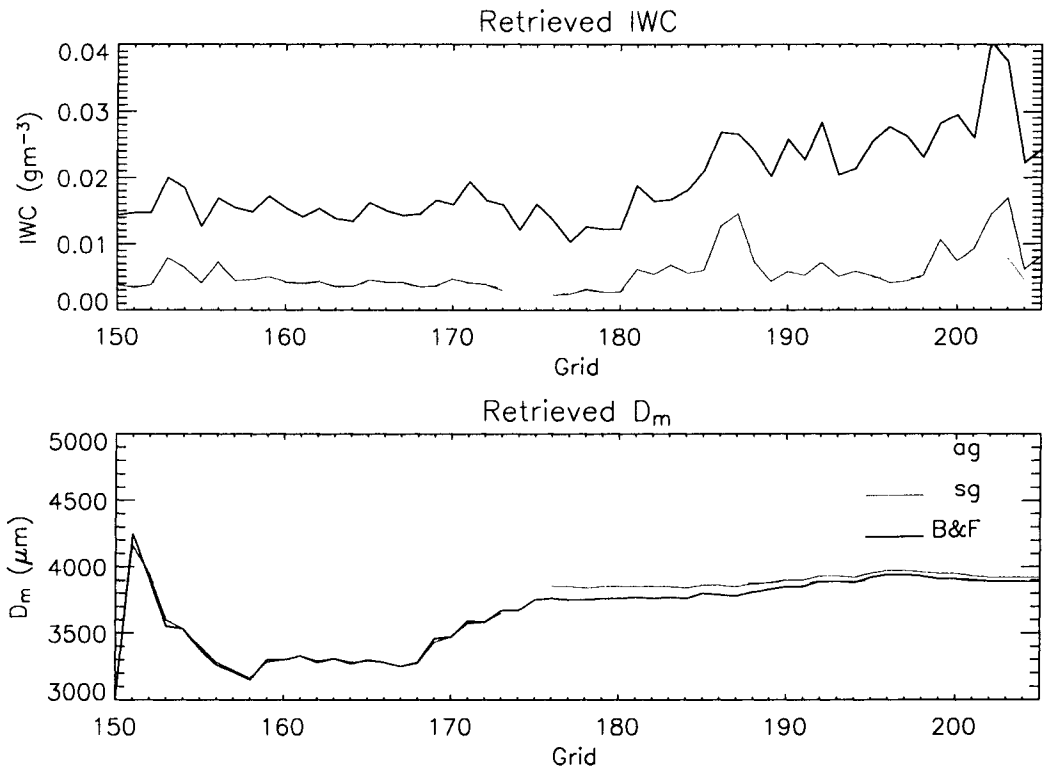

Figure 8.1. Ice water content and mean volume diameter as retrieved by the all-grid (ag), single-grid (sg) and default (B&F) assumption retrievals.

The all-grid optimal retrieval produced reasonable cloud-wide values for particle nonsphericity and density. Forward modeling of the *in situ* data using these optimal all-grid parameters produced an excellent match in the mean reflectivity for the cloud at the aircraft flight level and an RMS of only 2.9, 2.1 and 2.1 dBZ at 13.4, 35.6, and 94.9 GHz. However, the all-grid retrieval could not capture any trends in nonsphericity or density across the cloud.

The single-grid retrieval produced an excellent match of the **F(x)** to the observations, including any maxima, minima, and trends. It accomplished this by allowing the retrieved parameters to vary as necessary and the result is a volatile density parameter across the flight track. The unphysical nature of this variance across the horizontal structure of the cloud implied that the retrieval is using the density as a 'tuning knob' to match the remote sensing observations at individual grid points. However, in the cloud mean sense, the single-grid optimal parameters are close to the all-grid retrieved optimal parameters. There is a negative bias in the single-grid **F**(x) at 94.9 GHz that could indicate a problem with the *in situ* data such as undercounting at the lower sizes or the discontinuity between the 2DC and 2DP number concentrations.

Finally, the use of the optimal density and aspect ratio as improved assumptions in the forward model significantly improved the PSD retrieval in the cloud. The retrieved gamma PSD very closely matched the *in situ* PSD except for the smallest particles where the retrieved PSD indicated a higher number concentration. Since the optimally retrieved density and aspect ratio were derived to best fit the forward-modeled *in situ* to the remote sensing observations, it was no surprise that the PSD retrieval would improve, i.e., the retrieved PSD would look more like the *in situ*. However, the level of improvement was striking. The cloud probe data has been used to improve the PSD retrieval by improving the assumptions in the forward model but the retrieved PSD also does not show the undercounting of small particles that is characteristic of the 2D cloud probes in order to retain agreement with the 94.9-GHz radar reflectivities.

8.2 Vertical Profile PSD Retrieval

The clear sky case provides an excellent illustration of one of the strengths of the optimal estimation methodology. The non-convergence of the original retrieval indicated an inconsistency in one of the inputs: observations, input uncertainties, or forward model. The physical consistency enforced through the radiative transfer model ensures that any miscalibration across sensors or erroneous assumptions will result in failure of the retrieval to converge to a solution. In a traditional retrieval that uses only a brightness temperature (TB) differencing scheme, instead of simultaneously solving the radiative transfer for each frequency, this type of miscalibration error may have gone unnoticed.

The first thing to notice in the ice cloud retrieval is the microphysical nature of the cloud retrieved (Figures 7.2 and 7.3). The shape of the retrieved profile of μ shows a trend for μ to increase from the base towards the top. This trend is better defined in the optimal retrieval. At the edges (base and top) of the cloud the observations naturally provide less information about the cloud and the retrieval tends toward the *a priori* values, $\mu = -1.1$. A more negative μ indicates a more super-exponential gamma distribution such that the small particle tail of the distribution goes to increasing number concentrations. Thus, a more negative μ in general indicates a greater concentration of small particles. Also evident in Figures 7.2 and 7.3 is the trend towards greater N_o^* from the base to the top of the cloud and the trend towards greater D_m from top to base. These trends are consistent with particle growth processes where there would be more numerous, smaller particles at the top of the cloud and fewer but larger particles at cloud base.

Although the trends are evident in both the default and optimal retrieval profiles, they are more distinct in the optimal retrieval. Other differences are evident between the default and optimal retrieved profiles. The optimal retrieval shows more negative μ, larger D_m and smaller N_o^* than the default retrieval. These changes in the optimal model retrieval are the result of improving the model assumptions to better match the *in situ* PSD in chapter six. These differences in the PSD combined with the optimal assumptions of a greater density for smaller particles and oblate spheroids of a smaller volume for the same diameter produce a dramatically smaller IWC for the optimal retrieval. For the representative grid point, the optimal retrieval produces an IWC smaller by over an order

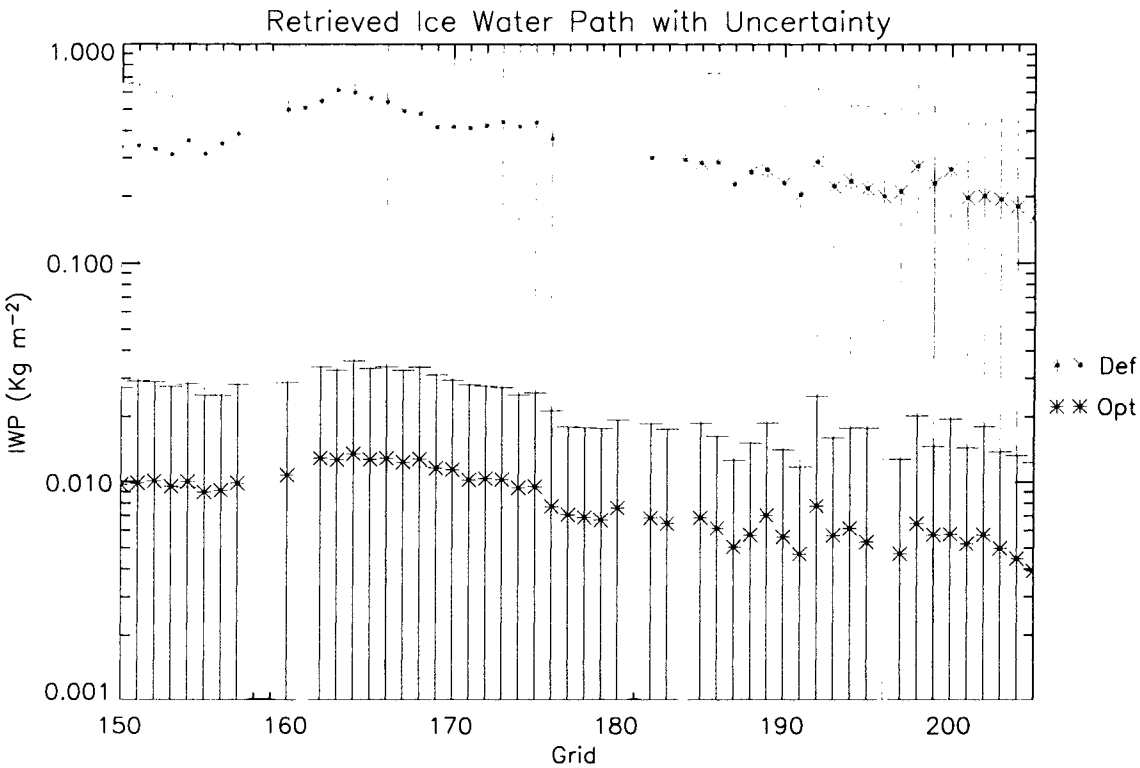

Figure 8.2. Retrieved ice water path for both default (Def) and optimal (Opt) cloud ice retrievals with error bars describing the uncertainty around the retrieved states.

of magnitude. The retrieved ice water path across the cloud is shown for both default and optimal cases in Figure 8.2 and illustrates the differences in ice water across the cloud.

The error bars in Figure 8.2 give the reason the two retrievals can produce such vastly different ice water contents/paths while still matching the observations. An error propagation model was constructed to calculate the uncertainty in computed IWP from the retrieved uncertainty (using the standard deviation as representative uncertainty) in the PSD parameters. The retrieved IWP and respective retrieved uncertainty for both default and optimal retrievals is shown and it is evident in the figure that the IWP uncertainty is very large for the default retrieval and has been significantly reduced for the optimal retrieval. Further inspection reveals that the default and optimal IWP PDFs overlap and that, for the vast majority of grid points, the optimally retrieved mean IWP falls within the default PDF. In other words, the characteristic (mean) retrieved state (here IWP) for the improved retrieval falls within the relatively wide PDF of default-retrieved states. However, the characteristic state for the default retrieved IWP does not fall within the much narrower PDF of improved retrieval states.

The differences between the default and optimal cases can be examined in greater detail by looking at a single-grid point retrieval. Tables 7.4 and 7.7 reveal that the two retrievals produce the same results in state parameters governing the background emission. But Tables 7.5 and 7.8 detail the differences evident in Figures 7.2 and 7.3. There is a reduction in uncertainty in both the $\sigma\ \mu$ and $\sigma\ N_o^*$ from the default retrieval to the optimal retrieval. However, the uncertainty in D_m, given by $\sigma\ D_m$ increases from default to optimal retrieval. Examining the **A**-matrix values yields results consistent with the changes in uncertainty. The optimal retrieval relies much more heavily on the

observations for both μ and N_o^* than the default retrieval. This important result is due to the optimization of the forward radiative transfer model in chapter six. The model improvement was based on best matching the forward modeling of the *in situ* PSD at all three radar observation frequencies. Intrinsic to this procedure was ensuring physical consistency across the suite of radar frequencies thus reducing the uncertainty in the forward modeling of the PSD. This reduction in uncertainty is now evident in the ability of the optimal retrieval to use the observations to determine μ and N_o^* rather than default to the *a priori* in situations where the default model could not match all three frequencies. Also evident is the trend towards more reliance on the *a priori* than the observations at the base and top of the cloud due to a lack of information when one or both of the APR-2 radars drop out.

The difference between the optimal and default retrievals is also evident in the information content analysis. The χ^2 for both retrievals is effectively the same, indicating that the fit of the forward modeled retrieved state, $\mathbf{F(x)}$ to the observations $\mathbf{y}$ is the same. However, the reduction in retrieval uncertainty in the optimal retrieval is dramatically reflected in the information content. The Shannon Information Content of the default retrieval was 124 while for the optimal retrieval $H = 211$. This indicates that the optimal retrieval is able to resolve 2^{87} more retrieved states than the default retrieval. So, although the two retrievals converge to answers that result in almost equivalent 'fits' to the observations, the resultant retrieval uncertainty in the default retrieval is required to be much larger to achieve this fit. The increased internal physical consistency in the forward model provided by the optimal assumptions results in the observations mapping into a smaller area in state space. The dominant contribution to the information content of the

retrieval comes from the N_o^* parameter and secondarily from the D_m. This is a slight shift from the default retrieval where the D_m showed more information content than in the optimal retrieval, consistent with the shift in retrieved uncertainty. Also consistent with the retrieved uncertainty is the lack of information around the edges of the cloud where one or more of the radars have no returns. In addition, the information content of the emission state parameters is relatively low, especially the surface emission parameters T_{sfc} and V_{sfc}. This is consistent with the absence of lower frequency microwave observations after the exclusion of the PSR data. It also shows that there is still some information about those parameters remaining in the higher frequency MIR data.

CHAPTER 9

CONCLUSIONS

The integration of radar observations over multiple frequencies with simultaneous *in situ* cloud probe observations through the use of a radiative transfer model represents a 'physical validation' of the measurements and model. The radiative transfer model enforces physical consistency between the observations. What these results indicate is that common assumptions about uncertainties from both observations and model have a major impact on the retrieval. The uncertainty due to the difference between 2DC and 2DP observed PSDs is shown to produce up to a 10 dBZ difference in **F(x)** at 94.9 GHz. The model assumptions of spherical particles and a Brown and Francis size-density relationship produce an RMS of 6, 8 and 12 dBZ at 13.4, 35.6 and 94.9 GHz when compared to the observations.

Even with an abundance of data the single-level retrieval uncertainty remained large but was now quantifiable through the optimal estimation method. A focus on reducing uncertainty from noise in sensors through additional calibration and cross calibration can help to reduce one of the sources of input uncertainty in the retrieval process.

For the ice cloud under study, the use of multiple complementary airborne remote sensing and *in situ* observations through an optimal estimation framework was able to determine an optimal ice size-density relationship of $\rho(D) = 0.07 * D^{-1.58}$ and oblate spheroid aspect ratio of 0.53. The use of these improved model assumptions in the PSD retrieval was able to fully describe the particle size distribution of the ice cloud at the level of the *in situ* observations such that the agreement between modeled reflectivities and observed reflectivities increased from +/- 6-12 dB to +/- 2–3 dB at all frequencies. These improved model assumptions were then incorporated into the model for the retrieval of a full vertical profile of hydrometeors.

For the vertical profile PSD retrieval, eleven passive microwave radiometer channels were combined with observations from three different radar frequencies to retrieve atmospheric profiles of an ice cloud. The different observations were integrated with each other and solved simultaneously through a forward radiative transfer model. The physical consistency enforced by this method identified a bias in one of the passive microwave instruments through the non-convergence of the retrieval.

The retrieval allowed all three parameters of a normalized gamma PSD to vary from level to level vertically through the cloud to gain information about the vertical microphysical structure of the cloud. However, even with the final observation suite of seven radiometer channels and three different radars, there was not enough information in the observations to fully determine all three parameters of the PSD at every level in the cloud. But, allowing all three PSD parameters to vary from level to level in the vertical enabled the algorithm to retrieve vertical cloud microphysical structure. The retrieval identified profiles of smaller, more numerous ice particles at the top of the cloud and

fewer but larger particles at cloud base. These results are consistent with cloud particle growth processes.

The effect of the model improvements from the single-level 'physical validation' was measured by the diagnostics inherent in the optimal estimation method. The optimal estimation diagnostics and information content analysis identified that, although both the default and the improved assumption retrievals were able to closely match the observations, the default retrieval was only able to do so with very large resultant uncertainties. The improved assumption model showed a significant decrease in the uncertainty and, consequently, a major increase in the information content of the retrieval. The result was that the default assumption retrieval produced an ice water content over an order of magnitude larger than the optimal retrieval. This difference was reconciled through the observation that the default retrieved state had such large uncertainty that the PDF of retrieved possible states was large enough to contain the optimal assumption retrieved state. However, the optimal assumption retrieval had much less uncertainty, such that the default-retrieved state was excluded from the improved retrieval PDF of retrieved states. The optimal estimation retrieval methodology provides an ideal framework for integrating multiple disparate observations to reduce or improve the assumptions required in the satellite cloud and rain retrieval process and to produce a quantitative uncertainty estimate while simultaneously diagnosing where future areas for improvement lie.

Observations of ice clouds are highly uncertain, even with data from three radars and seven high-frequency microwave radiometer channels. While the retrieval standard deviation appears quite large, this retrieval is operating without many of the *a priori*

assumptions made in operational algorithms. Operational retrievals must make those *a priori* assumptions when they operate in an environment lacking prior knowledge of the observed target and the breadth of data available in this study. But, the accuracy of the retrieval is impacted by the accuracy of the *a priori*, as shown in this paper. In the single-level validation retrieval, the *in situ* aircraft observations serve as an *a priori* source of information to refine the physical model used in the ice cloud retrieval. In the vertical profile PSD retrieval, the improved ice cloud model makes a significant impact on both the retrieved PSD and the resultant uncertainty. Despite the large retrieval uncertainty, this paper demonstrates that prior knowledge of the microphysics of the ice cloud (e.g., density and shape) is important for the accuracy of satellite retrievals. These sort of physical studies appear very worthwhile to reduce both the uncertainty and bias from future satellite missions such as CloudSat.

REFERENCES

AMSR Rainfall Validation Implementation Strategy 2001-2005, Draft, 2002.

Atlas, D., S. Y. Matrosov, A. J. Heymsfield, M-D. Chou, and D. B. Wolff, 1995: Radar and Radiation Properties of Ice Clouds. *J. Appl. Meteor.*, 34, 2329-2345.

Austin, R. L., and G. L. Stephens, 2001: Retrieval of stratus cloud microphysical parameters using millimeter-wave radar and visible optical depth in preparation for CloudSat. *J. Geophys. Res.*, **106**, 28,233-28,242.

Barber, P. W., and S. C. Hill, 1990: *Light Scattering by Particles: Computational Methods*, 261pp.

Benedetti, A., G. L. Stephens, and J. M. Haynes, 2003: Ice cloud microphysics retrievals from millimeter radar and visible optical depth using an estimation theory approach. *J. Geophys. Res.*, **108**,.

Berg, W., C. Kummerow, and C. Morales, 2002: Differences between east and west pacific rainfall systems. *J. Climate*, **15**, 3659-3672.

Bohren, C. F., and L. J. Battan, 1982: Radar backscattering of microwaves by spongy ice spheres. *J. Atmos. Sci.*, **39**, 2623-2629.

Brown, P. R. A., and P. N. Francis, 1995: Improved measurements of the ice water content in cirrus using a total-water probe. *J. Atmos. Ocean. Tech.*, **12**, 410-414.

Frisch, A. S., G. Feingold, C. W. Fairall, T. Uttal, and J. B., Snider, 1998: On cloud radar and microwave radiometer measurements of stratus cloud liquid water profiles. *J. Geophys. Res.*, **103**, 23195-23,197.

Heymsfield, A. J., A. Bansemer, C. Schmitt, C. Twohy, and M Poellot, 2004: Effective Ice Particle Densities Derived from Aircraft Data. *J. Atmos. Sci.*, **61**, 982-1003.

_____, S. Lewis, A. Bansemer, J. Iaquinta, L. M. Milosevich, M. Kajikawa, C. Twohy, and M. Poellot, 2002: A General Approach for Deriving the Properties of Cirrus and Stratiform Ice Cloud Particles. *J. Atmos. Sci.*, **59**, 3-29.

Kummerow, C., 1993: On the accuracy of the Eddington approximation for radiative transfer in the microwave frequencies. *J. Geophys. Res.*, **98**, 2757-2765.

_____, Y. Hong, W. S. Olson, S. Yang, R. F. Adler, J. McCollum, R. Ferraro, G. Petty, D. B. Shin, and T. T. Wilheit, 2001: The evolution of the Goddard Profiling algorithm (GPROF) for rainfall estimation from passive microwave sensors. *J. Appl. Meteor.*, **40**, 1801-1820.

L'Ecuyer, T. S., and G. L. Stephens, 2002: An estimation-based precipitation retrieval algorithm for attenuating radars. *J. Appl. Meteor.*, **41**, 272-285.

_____, C. Kummerow, and W. Berg, 2004: Toward a Global Map of Raindrop Size Distributions. Part I: Rain-Type Classification and Its Implications for Validating Global Rainfall Products. *J. Hydromet.*, **5**, 831-849.

_____, P. Gabriel, K. Leesman, S. J. Cooper, and G. L. Stephens, 2005: Objective Assessment of the Information Content of Visible and Infrared Radiance Measurements for Cloud Microphysical Property Retrievals over the Global Oceans. Part I: Liquid Clouds. *J. Appl. Meteor.*, IN PRESS.

Liou, K. N., 2002: *An Introduction to Atmospheric Radiation.* Academic Press, 583pp.

Masunaga, H. and C. Kummerow, 2005: Combined Radar and Radiometer Analysis of Precipitation Profiles for a Parametric Retrieval Algorithm. *J. Atmos. and Ocean. Tech.*, **22**, 909-929.

Maxwell-Garnett, J. C., 1904: Colors in metal glasses and in metallic films. *Philos. Trans. Roy. Soc. London*, **203A**, 385-420.

Piepmeier, J.R., and A. J. Gasiewski, 1996: Polarimetric Scanning Radiometer for Airborne Microwave Imaging Studies, *Proceedings of the 1996 International Geoscience and Remote Sensing Symposium*, 1688-1691, Lincoln, NE, May 27-31, 1996a.

Racette, P., R. F. Adler, J. R. Wang, A. J. Gasiewski, D. M. Jakson, and D. S. Zacharias, 1996: An Airborne Millimeter-Wave Imaging Radiometer for Cloud, Precipitation, and Atmospheric Water Vapor Studies. *J. Atmos. and Ocean. Tech.*, **13**, 610-619.

Roberti, L., J. Haferman, and C. Kummerow, 1994: Microwave radiative transfer through horizontally inhomogeneous precipitating clouds, *J. Geophys. Res.*, 99, 16707-16718.

Rodgers, C. D., 2000: *Inverse Methods for Atmospheric Sounding: Theory and Practice.* World Scientific, 238pp.

Sadowy, G. A., A. C. Berkun, W. Chun, E. Im, and S. L. Durden, 2003: Development of an advanced airborne precipitation radar, *Microwave J.*, **46**, 84-98.

_____, R. E. McIntosh, S. J. Dinardo, S. L. Durden, W. N. Edelstein, F. K. Li, A. B. Tanner, W. J. Wilson, T. L. Schneider, and G. L. Stephens, 1997: The NASA DC-8 airborne cloud radar: design and preliminary results, *Proceedings of IGARSS '97*, **4**, 1466-1469.

Smith, E. A., P. Bauer, F. S. Marzano, C. D. Kummerow, D. McKague, A. Mugnai, and G. Panegrossi, 2002. Intercomparison of microwave radiative transfer models for precipitating clouds, *IEEE: Trans. Geoscience & Rem. Sensing*, **40**, 541-549.

Testud, J., S. Oury, R. A. Black, P. Amayenc, and X. Dou, 2001: The Concept of "Normalized" Distibution to Describe Raindrop Spectra: A Tool for Cloud Physics and Cloud Remote Sensing. *J. Appl. Meteor.*, **40**, 1118-1140.

Ulaby, Fawwaz T., R. K. Moore, and A. K. Fung, 1981: *Microwave Remote Sensing, Active and Passive, Volume 1: Microwave Remote Sensing Fundamentals and Radiometry.* Artech House, 456 pp.

Viltard, N., C. Kummerow, W. S. Olson, and Y. Hong, 2000: Combined use of the radar and radiometer of TRMM to estimate the influence of drop size distribution on rain retrievals. *J. Appl. Meteor.*, **39**, 2103-2114.

Wilheit, T. T., 1979: The Effect of Wind on the Microwave Emission From the Ocean's Surface at 37 GHz. *J. Geophys. Res.*, **48**, 4921-4926.

APPENDIX A

JPL CORRECTION

Early retrievals showed a high bias in the **F(x)** relative to the observations, especially at 35.6 GHz. Though the retrieval found an optimal solution state, the result did not match all three frequencies. The optimal retrieved state consistently produced a positive bias in the 35.6 GHz and to a lesser extent in the 13.4 GHz in an attempt to match the 94.9 GHz given the supplied *in situ* data. When the retrieval was performed without the 94.9-GHz data, it was able to successfully converge to a solution with almost no bias in the APR-2 frequencies. In conversations with Dr. Simone Tanelli at the Jet Propulsion Laboratory (the source of the APR-2 data), he reported a problem with quantization in the APR-2 data at the lowest reflectivity values. These low reflectivities were exactly the data used in the ice cloud retrieval. JPL applied a nonlinear corrective factor to the APR-2 reflectivities and made available the corrected data. The effect of the correction was to increase reflectivities in both the 13.4 and 35.6 GHz relative to the pre-corrected data. This correction brought the observations more in line with what the retrieval was producing. Now, when the retrieval was performed on the corrected data, the solution state was impacted. Most importantly, the mean **F(x)** using the optimal retrieval parameters now had a greater separation between the 13.4 and 35.6 **F(x)**

reflectivities indicating a shift in the Rayleigh-Mie aspects of the particle size distribution. Additionally, the RMS around the retrieval had been reduced. Note especially that the mean **F(x)** at 94.9 GHz better matched the observations even though the ACR data is unchanged. This was indicative of increased physical consistency between the APR-2 and the ACR observations. This lack of physical consistency between the instruments was exactly what was seen in the original retrieval. The physical consistency enforced by the optimal estimation retrieval is one of the key benefits of the technique, and can be used to identify possible biases between instruments.

Pre-correction (x=1.8, 0.56; χ^2 = 152):

Frequency	**Observations**	**F(*in situ*)**	**RMS**
13.4 GHz	9.4 dBZ	8.4 dBZ	3.4 dBZ
35.6 GHz	4.7 dBZ	6.3 dBZ	2.8 dBZ
94.9 GHz	2.3 dBZ	1.3 dBZ	2.1 dBZ

Post-correction (x=1.6, 0.53; χ^2 = 109):

Frequency	**Observations**	**F(*in situ*)**	**RMS**
13.4 GHz	11.9 dBZ	11.6 dBZ	2.9 dBZ
35.6 GHz	8.3 dBZ	8.4 dBZ	2.1 dBZ
94.9 GHz	2.3 dBZ	2.4 dBZ	2.1 dBZ